Journal of Computational Physics **174,** 138–170 (2001)
doi:10.1006/jcph.2001.6884, available online at http://www.idealibrary.com on IDEAL®

Recent Advances in Models for Thermal Oxidation of Silicon

Krishna Garikipati*,[1] and Vinay S. Rao†,[2]

**Department of Mechanical Engineering, University of Michigan, Ann Arbor, Michigan 48109; and †Avanticorp, Fremont, California 94538*
E-mail: krishna@engin.umich.edu

Received June 6, 2000; revised June 25, 2001

Recent advances are presented in the models for thermal oxidation that have been been introduced by Rao and co-workers. The level-set formulation for movement of the Si–SiO_2 interface has been improved by the application of an efficient velocity–projection scheme for noninterface points. A penalty formulation has been introduced to enforce positive concentrations in the presence of discontinuities. The annealing-induced expansion of SiO_2 has been established as an important effect and a phenomenological relation has been identified for it. Inelastic volumetric strains have been proposed, evolution equations have been specified, and the underlying thermodynamics has been elucidated. The enhanced strain finite-element method has been applied to the inhomogeneous expansion of interface elements that have silicon and SiO_2 parts to them.

Key Words: diffusion; level-set methods; continuum mechanics of solids; thermodynamics of solids; finite elements.

1. INTRODUCTION

The recent work of Rao and Hughes [1] and Rao *et al.* [2] treated the problem of thermal oxidation of silicon in the framework of continuum balance laws and finite strain mechanics. Advanced finite-element formulations were also applied. This paper presents recent advances made on the above work. This introductory section is organized into passages that outline earlier models, the work of Rao and co-workers, and areas for possible advances over their models.

Thermal oxidation of silicon involves the following phenomena: (i) diffusion of oxidant through preexisting SiO_2, (ii) the oxidation reaction at the Si–SiO_2 interface, and

[1] At Center for Integrated Systems, Stanford University, Stanford, CA, at the time of this work.

[2] At Schlumberger Cambridge Research Centre, Cambridge, UK, at the time of this work.

0021-9991/01 $35.00

(iii) expansion associated with the large difference in molar volumes between Si and SiO_2. The diffusivity and reaction constants are stress-dependent. The stress arises from the expansion and depends on diffusion and reaction through the moving Si–SiO_2 interface and its delienation of Si and SiO_2 subdomains.

A Fickian model is employed for diffusion. Conventionally, the diffusing oxidant (O_2 or H_2O) was assumed to react fully at the interface, thus resulting in a discontinuity in oxidant concentration. Traditional approaches to the problem have involved the specification of a finite-element mesh, where element edges are aligned with the interface. Diffusion is solved for only over the SiO_2 subdomain and the movement of the interface is accomplished by movement of nodes (see Rafferty [3], Peng *et al.* [4], Senez *et al.* [5], Uchida *et al.* [6], Cea and co-workers [7, 8] and references therein). This approach has the undesirable consequence of requiring remeshing with every time step as the interface moves. Depending on the interface topology, it can lead to poor mesh quality. To remedy these drawbacks Rao *et al.* [2] have adopted the level-set formulation of Sethian and co-workers (see Sethian [9], Sethian and Adalsteinsson [10]) that uses a mathematical description of the interface and a partial differential equation for its motion. The interface velocity is derived from fundamental mass balance considerations (see Rao and Hughes [1]). The diffusion equation is solved over the silicon and SiO_2 subdomains, thus circumventing the limiting assumption of complete reaction of O_2 at the interface. Instead, the concentration segregation condition—which specifies the oxidant concentration on either side of the interface—is invoked and enforces a discontinuity in oxidant concentration at the interface. The level-set solution indicates the position of the interface which is allowed to lie within an element. This leads to a discontinuity in oxidant concentration within an element. A finite-element scheme based upon the method of incompatible modes is used to construct discontinuous local interpolations for oxidant concentration. With these formulations, the position and evolution of the interface is not dictated by the underlying spatial discretization, and remeshing is entirely eliminated as the interface evolves. Additionally, discontinuous concentrations are recovered, respecting the segregation condition.

Traditionally the mechanics accompanying thermal oxidation of silicon has been modeled under the infinitesimal strain approximation. Recognizing the tendency for SiO_2 to flow at temperatures exceeding approximately 750°C, material models involving various combinations of elasticity and viscosity have been used. Early work included the constant viscosity model of Chin [11], the linear Maxwell-viscoelastic model of Hsueh and Evans [12], and the "incrementally" linear elastic model of Needs *et al.* [13]. Later, Rafferty [3] replaced the constant viscosity with a stress-dependent, Eyring-viscosity model, which has subsequently been used by Hu [14], Fahey *et al.* [15], Uchida *et al.* [6], and Senez *et al.* [5]. More recently, Navi and Dunham [16] modeled the oxide as a viscous, compressible fluid, and Yu *et al.* [17] employed a viscosity varying linearly in time with a Maxwell-viscoelastic model.

The observation that an intrinsic stress is created by thermal oxidation was made by EerNisse [18]. Among the mechanisms of stress-generation that have been suggested are those based on shear strain by Pilling and Bedworth [19] and Vermilyea's [20] extension of Mott's notion of "kink-sites." According to this last-mentioned model, the expansion associated with oxidation is purely one-dimensional, in a direction perpendicular to the interface.

Wide-ranging objections can be raised to the above models of the mechanics of thermal oxidation of silicon. (i) The expansion associated with oxidation is finite. In fact, the molar volume of SiO_2 in a stress-free state is 2.2 times that of silicon, rendering the infinitesimal

strain approximation invalid. (ii) The rate-dependent material models mentioned above for SiO_2 are viscous or, at best, Maxwell-viscoelastic and thus model fluidlike behavior. In the absence of flow, the stress in these models vanishes. This contradicts experimental observations such as those of EerNisse [18] and, more recently, Yu *et al.* [17], where a nonvanishing stress is measurable even in the absence of oxide flow. Solidlike behavior must therefore be incorporated [i.e., the stress must depend on the deformation in addition (possibly) to the rate of deformation]. The experiments of Yu *et al.* [17] also indicate that the viscosity and moduli of SiO_2 decrease at higher temperatures and fluidlike behavior is approached. Therefore there is a need for material models that span the range between solid and fluidlike behavior. These models must demonstrate temperature-dependent material properties. (iii) The one-dimensional model of oxide-expansion is fundamentally incapable of reproducing the results of water curvature experiments. In the experiments of EerNisse [18] and Yu *et al.* [21], thin films of SiO_2 were thermally grown on silicon substrates. The associated expansion forces the wafer to bend away from the film surface. Such a phenomenon is reproducible only if lateral expansion of the film is accounted for. The calculations are based on simple principles of Euler–Bernoulli bending and underlie the widely used Stoney's formula (see Stoney [22]). These observations indicate that proper modeling of the kinematics associated with oxidation must account for three-dimensional oxide expansion. (iv) The actual expansion of newly formed SiO_2 is represented by enforcing the movement of the corresponding nodes in the finite-element mesh. There is no representation of the expansion at the constitutive level.

In the work of Rao and Hughes [1] the nonlinear finite strain theory provides the underlying description of mechanics. Thus the large expansion ratios associated with oxidation are treated accurately. A standard solid viscoelastic model (see Simo and Hughes [23]) has been adopted for SiO_2. This allows representation of the entire range of material behavior from viscous fluid, to Maxwell-viscoelastic fluid, to viscoelastic solid by appropriate choice of parameters (see Garikipati *et al.* [24] for details). The full three-dimensional expansion of SiO_2 is modeled. Thus, wafer curvature during thermal oxidation is reproduced. Additionally, the expansion is modeled via the constitutive equations and not ad hoc movement of mesh nodes.

The course of development of the above work pointed out several aspects where advances were either possible or needed. Attention is turned to them in the present paper. Among these are the following. (i) The evolution of the level set that describes the interface is governed by a partial differential equation, which is defined throughout the domain. However mass-balance considerations provide a Rankine–Hugoniot–type relation for interface velocity that holds only at the interface. The level-set velocity at points not lying on the interface must be determined through other means. (ii) The discontinuity-resolving interpolations employed for solution of the diffusion equation have been observed to lead to negative concentrations in certain situations. This is clearly nonphysical, and numerical schemes that preserve positive concentrations are needed. (iii) The oxide displays a density relaxation when annealed at high temperatures. This can also be modeled as an expansion in addition to that associated with oxidation. (iv) The expansion of SiO_2, while modeled at the constitutive level, left unaddressed the nature of the strains associated with expansion, a complete statement of the thermodynamics of these expansions, and the derivation of the stress–strain relations from the second law. (v) Unsatisfactory numerical performance was observed in certain instances in the solution of the mechanics. This has been related to the highly inhomogeneous nature of the hydrostatic component of the constitutive relationship in elements that consist of silicon and SiO_2 parts. The element-level kinematics in Rao *et al.* [2] is incapable of representing

the associated discontinuous strains. Finite-element methods that remedy this difficulty by allowing discontinuous strains at the element-level are thus indicated.

The organization of the remaining sections of this paper is as follows. Section 2 outlines the level-set formulation and discusses improvements to velocity calculations for this purpose. Section 3 provides a treatment of the mechanics, paying particular attention to a phenomenological model for annealing-induced expansion of SiO_2 and to a reformulation of expansion in terms of inelasticity and thermodynamics. Recently developed numerical methods for level-set evolution, diffusion-reaction, and inhomogeneous expansion are described in Section 4. Section 5 contains numerical examples demonstrating the new numerical methods, and Section 6 makes closing remarks.

2. LEVEL-SET FORMULATION FOR A MOVING INTERFACE

We begin with an overview of the level-set method applied to evolution of a bimaterial interface.

2.1. Overview

Consider a body Ω, open in $\mathbb{R}^{n_{\text{dim}}}$ ($n_{\text{dim}} = 2, 3$ are the cases of interest) and a surface $\Gamma \subset \Omega$, where Γ is an $n_{\text{dim}} - 1$-dimensional manifold. It is assumed that Γ separates Ω into disjoint subsets Ω^- and Ω^+, open in Ω such that $\Gamma \cap \Omega^- = \emptyset$, $\Gamma \cap \Omega^+ = \emptyset$, and $\overline{\Omega} = \overline{\Omega^- \cup \Gamma \cup \Omega^+}$ (Fig. 1). A parametrization of Γ as a level set of an $n_{\text{dim}} + 1$-dimensional hypersurface is introduced via the function $\phi(\boldsymbol{x}, t)$, where, $\boldsymbol{x} \in \mathbb{R}^{n_{\text{dim}}}$ is the position vector of a material point and t represents time. The $n_{\text{dim}} + 1$-dimensional hypersurface is parameterized by $(\phi, \boldsymbol{x}) \in \mathbb{R} \times \mathbb{R}^{n_{\text{dim}}}$. Without loss of generality Γ is defined as the zero level-set of ϕ, or

$$\Gamma_t := \{\boldsymbol{x} \in \Omega \mid \phi_t(\boldsymbol{x}) = 0\} \, \forall \, t \geq 0. \tag{1}$$

The above description is made more precise by specifying $\phi_t(\boldsymbol{x})$ to be the signed distance function

$$\phi_t(\boldsymbol{x}) := \begin{cases} \min\limits_{\boldsymbol{y} \in \Gamma_t} \|\boldsymbol{x} - \boldsymbol{y}\|: & \boldsymbol{x} \in \Omega_t^- \\ -\min\limits_{\boldsymbol{y} \in \Gamma_t} \|\boldsymbol{x} - \boldsymbol{y}\|: & \boldsymbol{x} \in \Omega_t^+, \\ 0: & \boldsymbol{x} \in \Omega_t \end{cases} \tag{2}$$

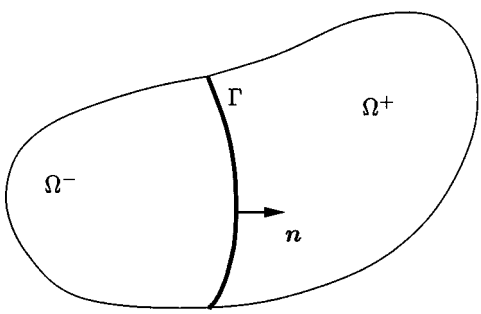

FIG. 1. A body $\overline{\Omega} = \overline{\Omega^- \cup \Gamma \cup \Omega^+}$ with interface Γ.

where $\|\cdot\|$ denotes the Euclidean norm. In this setting, the evolution of level-set contours is governed by the partial differential equation

$$\frac{\partial \phi}{\partial t} + \nabla\phi \cdot \boldsymbol{v} = 0, \tag{3}$$

where $\boldsymbol{v}$ is the velocity of the contour. Writing the velocity as

$$\boldsymbol{v} = v^M \boldsymbol{m} + v^N \boldsymbol{n}, \tag{4}$$

where $\boldsymbol{m}$ and $\boldsymbol{n}$ are, respectively, the unit tangent and unit normal to the contour $\phi_t(\boldsymbol{x}) = c$ (constant) and v^M and v^N are the corresponding components of $\boldsymbol{v}$, and using $n = \nabla\phi/\|\nabla\phi\|$, it follows that (3) can be written as

$$\frac{\partial \phi}{\partial t} + v^N \|\nabla\phi\| = 0. \tag{5}$$

The partial differential equation in (5) is a nonlinear advection equation.

The setting of reacting species was applied in Rao and Hughes [1] to the oxidation reaction

$$\mathrm{Si} + \mathrm{O}_2 \rightleftharpoons \mathrm{SiO}_2, \tag{6}$$

with the surface Γ representing a bimaterial interface at which the reactions take place. It was shown that the magnitude of the normal velocity is

$$v^N|_\Gamma = -\frac{[\![\boldsymbol{T}_{\mathrm{ox}} \cdot \boldsymbol{n}]\!]_\Gamma}{[\![\rho_{\mathrm{ox}}]\!]_\Gamma}, \tag{7}$$

with T_{ox} denoting the flux of SiO_2 molecules into the Si substrate, $\boldsymbol{n}$ being the normal to Γ directed into the Si region, and ρ_{ox} representing the concentration of SiO_2 at the interface. The symbol $[\![\bullet]\!]$ is used to indicate a jump in the corresponding quantity: $[\![\bullet]\!] = (\bullet)^+ - (\bullet)^-$. Under suitable assumptions, (7) can be cast in the form

$$v^N|_\Gamma = \frac{k_s \rho_i}{N_1}, \tag{8}$$

where N_1 is a constant representing the concentration of SiO_2 in Ω^-, ρ_i denotes concentration of O_2 at the interface, and k_s is a reaction constant for (6) defined by the relation

$$\boldsymbol{T}_{\mathrm{ox}} = k_s \rho_i \quad \text{at} \quad \Gamma. \tag{9}$$

The quantity ρ_i can be calculated by solving the problem for diffusion of O_2 through Ω coupled with the chemical reaction (6) at Γ (see Rao and Hughes [1]). In the present setting, the weak form of the diffusion problem is as follows.

$$\text{Find} \quad \rho \in \mathcal{S} = \{\rho \in \mathrm{L}_2(\Omega) \mid \rho = \rho_g \text{ on } \partial\Omega_\rho\} \tag{10}$$

$$\text{and} \quad \boldsymbol{T} = -D\nabla\rho \text{ in } \Omega \setminus \Gamma, \tag{11}$$

$$\text{such that} \quad \int_{\Omega\setminus\Gamma} \nabla w \cdot \boldsymbol{T}\, dV - \int_\Gamma w[\![\boldsymbol{T}\cdot\boldsymbol{n}]\!]\, ds = -\int_\Omega wf\, dV + \int_{\partial\Omega_h} w\bar{h}\, ds, \tag{12}$$

where w is the weighting function corresponding to ρ, f is a distributed source, ρ_g is the specified concentration on the boundary subset $\partial\Omega_\rho$, $\bar{h}$ is the specified normal component of oxidant flux on the boundary subset $\partial\Omega_h$, and $\overline{\partial\Omega} = \overline{\partial\Omega_\rho \cup \partial\Omega_h}$. The diffusivity D and the reaction constant k_s introduced above are, in general, stress-dependent. This dependence is discussed below. The conditions involving flux and concentration discontinuities at Γ provide the necessary coupling of the reaction with diffusion (see Rao and Hughes [1] for details).

2.2. Velocity Projection for the Level-Set Method

It is important to note that (7) and (8) hold for v^N only at the interface Γ_t. They do not provide a formula applicable throughout Ω. At points $\boldsymbol{x} \notin \Gamma_t$, v^N must be evaluated by other means.

The velocity extension method applied to the present problem is based upon the definition of $\phi_t(\boldsymbol{x})$ as a distance function. The following elementary observation can be made. Consider a point $\boldsymbol{x}_\Gamma$ that lies on the interface Γ_{t_0} at time t_0 [i.e., $\phi_{t_0}(\boldsymbol{x}_\Gamma) = 0$]. Let the normal velocity of Γ_{t_0} be $v^N\boldsymbol{n}$ at $\boldsymbol{x}_\Gamma$. It follows that the level-set contour $\phi_{t_0}(\boldsymbol{y}) = c$ (constant) also moves with normal velocity $v^N\boldsymbol{n}$ for any point $\boldsymbol{y}$ such that the normal projection of $\boldsymbol{y}$ onto Γ_{t_0} is $\boldsymbol{x}_\Gamma$.

This property is used to exactly project the level-set velocity field to any point not lying on Γ. Section 4 discusses algorithms for this projection. The reader is directed to the work of Sethian and co-workers [9, 10, 25] and references therein for a comprehensive treatment of level-set methods, including velocity projection techniques.

3. MECHANICS OF THE THERMAL OXIDATION OF SILICON

This section begins with an overview of the setting for the mechanics of thermal oxidation (see the original work of Rao and Hughes [1] for details).

3.1. Overview

The finite strain formulation is adopted specifically to provide a proper treatment of the large expansion of thermally grown SiO_2.

Consider the body, Ω, open in $\mathbb{R}^3$ with material points $\boldsymbol{X} \in \mathbb{R}^3$ in a reference cartesian frame. The boundary of Ω is denoted $\partial\Omega$. Consider a one-parameter set of current configurations $\varphi_t(\Omega)$ representing the deformation of Ω. Under the point-to-point map, $\varphi_t(\boldsymbol{X})$, material points are carried from the reference to current placement: $\boldsymbol{X} \mapsto \varphi_t(\boldsymbol{X})$. One writes

$$\boldsymbol{x}(t) = \boldsymbol{X} + \boldsymbol{u}(\boldsymbol{X}, t), \quad \varphi(\boldsymbol{X}, t) \equiv \boldsymbol{x}(t), \tag{13}$$

where $\boldsymbol{u} \in \mathbb{R}^3$ is the displacement vector. The deformation gradient tensor, $\boldsymbol{F} \in \mathbb{GL}(3)$ (the space of 3×3 matrices), is introduced,

$$\boldsymbol{F}_t = \frac{\partial \varphi_t}{\partial \boldsymbol{X}}, \tag{14a}$$

$$= \mathbf{1} + \frac{\partial \boldsymbol{u}_t}{\partial \boldsymbol{X}}, \tag{14b}$$

and is positive definite; accordingly, its determinant $J = \det[\boldsymbol{F}]$ remains positive. This

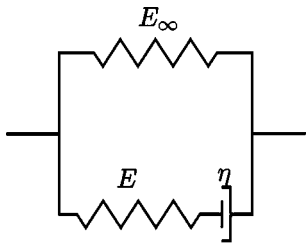

FIG. 2. Schematic representation of the standard solid viscoelastic model for the one-dimensional case.

condition is the local impenetrability of matter. In (14b), **1** is the second-order identity tensor. The kinematics are described in the reference configuration via the right Cauchy–Green tensor, $\boldsymbol{C} = \boldsymbol{F}^T\boldsymbol{F}$, where $\boldsymbol{C} \in \mathbb{S}(3)$ (the space of symmetric 3×3 matrices). At the outset, the following volumetric/deviatoric decomposition is adopted following Simo *et al.* [26]:

$$\boldsymbol{F} = J^{1/3}\bar{\boldsymbol{F}}. \tag{15}$$

Clearly, $\bar{\boldsymbol{F}}$ is volume-preserving. Corresponding to $\bar{\boldsymbol{F}}$ we define $\bar{\boldsymbol{C}} := J^{-2/3}\boldsymbol{C}$.

The constitutive model is introduced next. The standard solid model of viscoelasticity [27] is adopted for the oxide. A schematic representation of the model in terms of springs and viscous dashpots in the one-dimensional, infinitesimal strain case appears in Fig. 2. This model also makes an appearance in the literature under the name the "Poynting–Thomson Model" [28]. The compressible Neo–Hookean-stored energy function (see Ciarlet [29]) is modified to incorporate the standard solid viscoelastic model as follows:

$$\psi(J, \bar{\boldsymbol{C}}, \boldsymbol{Q}) = \frac{1}{2}\kappa(\log[J])^2 + \frac{1}{2}\mu[\bar{\boldsymbol{C}} : \mathbf{1} - 3] - \frac{1}{2}\boldsymbol{Q} : (\bar{\boldsymbol{C}} - \mathbf{1}) + \psi_I(\boldsymbol{Q}). \tag{16}$$

In the above function, $\boldsymbol{Q}$ is a stresslike variable that models the viscoelastic response through the equations

$$\begin{aligned} &\dot{\boldsymbol{Q}} + \frac{1}{\tau}\boldsymbol{Q} = \frac{\gamma}{\tau}\mathrm{DEV}\left[2\frac{\partial \bar{W}^\circ}{\partial(\boldsymbol{C})}\right], \\ &\lim_{t\to-\infty} \boldsymbol{Q} = 0, \end{aligned} \tag{17}$$

where the parameter γ is a nondimensional modulus, τ is a relaxation time, $\mathrm{DEV}[(\bullet)]$ is the deviatoric operator for contravariant tensors in the reference configuration,

$$\mathrm{DEV}[(\bullet)] := (\bullet) - \frac{1}{3}[(\bullet) : \boldsymbol{C}]\boldsymbol{C}^{-1}, \tag{18}$$

and the stored energy function has been decoupled to write

$$\bar{W}^\circ(\bar{\boldsymbol{C}}) = \frac{1}{2}\mu[\bar{\boldsymbol{C}} : \mathbf{1} - 3] - \frac{1}{2}\boldsymbol{Q} : (\bar{\boldsymbol{C}} - \mathbf{1}) + \psi_I(\boldsymbol{Q}). \tag{19}$$

Equations (17) can be solved to provide a convolution integral for $\boldsymbol{Q}$:

$$\boldsymbol{Q}(t) = \frac{\gamma}{\tau} \int_{-\infty}^{t} \exp[-(t-s)/\tau]\, \mathrm{DEV}\left\{ 2\frac{\partial \bar{W}^{\circ}(\bar{\boldsymbol{C}}(s))}{\partial \boldsymbol{C}} \right\} \mathrm{d}s. \tag{20}$$

The function $\psi_I(\boldsymbol{Q})$, at equilibrium, is written as

$$\psi_I(\boldsymbol{Q}) = -\gamma \frac{1}{2}\mu[\bar{\boldsymbol{C}} : \mathbf{1} - 3] + \frac{1}{2}\boldsymbol{Q} : (\bar{\boldsymbol{C}} - \mathbf{1}) \tag{21}$$

and provides the proper conditions at thermodynamic equilibrium. The symbols κ and μ are, respectively, the bulk and shear moduli. Details are provided in [23]. The second Piola–Kirchhoff stress is now calculated as

$$\boldsymbol{S} = 2\frac{\partial \psi}{\partial \boldsymbol{C}}, \tag{22}$$

which is related to the Cauchy stress, $\boldsymbol{\sigma}$, by $\boldsymbol{S} = \boldsymbol{F}^{-1} J \boldsymbol{\sigma} \boldsymbol{F}^{-T}$ and to the nominal stress, $\boldsymbol{P}$, by $\boldsymbol{P} = \boldsymbol{F}\boldsymbol{S}$.

An important feature of the present viscoelastic model is that the viscoelastic, stresslike variable $\boldsymbol{Q}$, is driven by the deviatoric component of the stress, as is apparent in (17). Conversely, only the deviatoric stress demonstrates viscoelastic relaxation. This can be seen by applying (22) to (16) and using (18)–(21).

The law of mechanical equilibrium for the quasistatic case is written as

$$\mathrm{DIV}[\boldsymbol{P}] + \boldsymbol{f} = 0, \tag{23}$$

where $\boldsymbol{f}$ denotes the body force. Boundary conditions are specified as

$$\boldsymbol{u}|_{\partial\Omega_u} = \boldsymbol{g}, \quad \boldsymbol{P}\boldsymbol{F}^T\boldsymbol{n}|_{\partial\Omega_t} = \bar{\boldsymbol{t}}, \tag{24}$$

where $\partial\Omega_u$ and $\partial\Omega_t$ are, respectively, those subsets of $\partial\Omega$ with displacement and traction boundary conditions specified.

3.2. Inelastic Volume Change

The thermal oxidation of silicon involves a local volume change of 120% arising from the large difference in unconstrained molar volumes of Si and SiO_2. In this work, the expansion is assumed to occur instantaneously when a Si atom is oxidized. Experiments by Irene *et al.* [30] have revealed that when SiO_2 is annealed at temperatures above 650°C, the density undergoes a gradual relaxation. It is of importance that both the volume changes mentioned here are independent of the prevailing state of stress. Other processes drive them: in the first case, oxidation, and in the second, a structural change activated by temperature. The chemical reaction of oxidation in (6) is sufficiently exothermic to be regarded as irreversible. The energy of reaction is approximately −700 kJ per mol at a typical oxidation temperature of 1000°C (see De Hoff [31], pp. 326–327), almost double that for the oxidation $2H_2 + O_2 \rightleftharpoons 2H_2O$. The corresponding volume change will be treated as irreversible. The density of SiO_2 that has been annealed at higher temperatures is not found to increase again on lowering the temperature below 650°C. This volume change, too, can be treated as

irreversible. The total expansion, Θ, is represented as a composition of $\Theta^{\mathrm{i}}_{\mathrm{ox}}$ (for oxidation) and $\Theta^{\mathrm{i}}_{\mathrm{a}}$ (for annealing).

$$\Theta^{\mathrm{i}} = \Theta^{\mathrm{i}}_{\mathrm{ox}}\Theta^{\mathrm{i}}_{\mathrm{a}}. \tag{25}$$

The inelastic volume expansion ratios $\Theta^{\mathrm{i}}_{\mathrm{ox}}$ and $\Theta^{\mathrm{i}}_{\mathrm{a}}$ are viewed as internal variables and evolution laws can be specified for them. For the component associated with the oxidation reaction, one has

$$\Theta^{\mathrm{i}}_{\mathrm{ox}}(t) = 1 + 1.2H(t - t_{\mathrm{ox}}), \tag{26}$$

where $H(t - t_{\mathrm{ox}})$ is the Heaviside function defined as

$$H(t - t_{\mathrm{ox}}) = \begin{cases} 0 : t - t_{\mathrm{ox}} < 0 \\ 1 : t - t_{\mathrm{ox}} \geq 0 \end{cases} \quad t_{\mathrm{ox}} > 0. \tag{27}$$

An evolution equation for the annealing-related component can be obtained from the work of Taniguchi *et al.* [32]. The resulting expression, phenomenologically based, is

$$\Theta^{\mathrm{i}}_{\mathrm{a}}(t) = \frac{(n_0 - 1)^{\alpha}}{(n_\infty - 1 + (n_0 - n_\infty)\exp[-(t/\tau)^a])^{\alpha}}, \tag{28a}$$

$$\bar{\tau}(T) = \bar{\tau}_0 \exp(E_A/kT), \tag{28b}$$

$$\bar{\tau}_0 = 1.26 \times 10^{-21}\,\mathrm{s}, \tag{28c}$$

$$E_A = 6\,\mathrm{eV}, \tag{28d}$$

where n is the refractive index, k is the Boltzmann constant, T represents temperature in Kelvin, and subscripts $(\cdot)_0$ and $(\cdot)_\infty$ refer to initial and final values of the corresponding quantities. Suitable values of the exponents are $\alpha = 0.17$ and $a = 1.63$.

Having delineated the inelastic volume change, it follows that the elastic volume change ratio is simply

$$\Theta^{\mathrm{e}} = J/\Theta^{i}. \tag{29}$$

Accordingly, a further modification of the stored energy function (16) is required to arrive at a constitutive model incorporating the inelastic volume change ratio. The stored energy function is rewritten as

$$\bar{\psi}(\Theta^{\mathrm{e}}, \bar{\boldsymbol{C}}, \boldsymbol{Q}) = \frac{1}{2}(\kappa \log[\Theta^{\mathrm{e}}])^2 + \frac{1}{2}\mu[\bar{\boldsymbol{C}} : \mathbf{1} - 1] - \frac{1}{2}[\boldsymbol{Q} : (\bar{\boldsymbol{C}} - \mathbf{1})] + \psi_I(\boldsymbol{Q}), \tag{30}$$

consistent with the notion that only elastic volumetric deformations contribute to the stored energy. Recourse can now be taken to a classical approach, namely, Coleman and Noll's argument (see Truesdell and Noll [33]), to arrive at the constitutive law for stress. The process makes crucial use of the Clausius–Planck inequality,

$$\mathcal{D} = \frac{1}{2}\boldsymbol{S} : \dot{\boldsymbol{C}} - \frac{\mathrm{d}}{\mathrm{d}t}\bar{\psi}(\Theta^{\mathrm{e}}, \bar{\boldsymbol{C}}, \boldsymbol{Q}) \geq 0, \tag{31}$$

where $\mathcal{D}$ denotes the rate of dissipation of energy and the first term on the right-hand side is the stress power. Using the decomposition $\boldsymbol{C} = \Theta^{\mathrm{e}^{2/3}}\Theta^{\mathrm{i}^{2/3}}\bar{\boldsymbol{C}}$ gives [see (15) and (29)]

$$\boldsymbol{S} : \frac{1}{2}\left[\frac{2}{3}\boldsymbol{C}\frac{\dot{\Theta}^{\mathrm{e}}}{\Theta^{\mathrm{e}}} + \frac{2}{3}\boldsymbol{C}\frac{\dot{\Theta}^{\mathrm{i}}}{\Theta^{\mathrm{i}}} + \Theta^{\mathrm{e}^{\frac{2}{3}}}\Theta^{\mathrm{i}^{\frac{2}{3}}}\dot{\bar{\boldsymbol{C}}}\right] - \frac{\partial\bar{\psi}}{\partial\Theta^{\mathrm{e}}}\dot{\Theta}^{\mathrm{e}} - \frac{\partial\bar{\psi}}{\partial\boldsymbol{C}} : \dot{\bar{\boldsymbol{C}}} - \frac{\partial\bar{\psi}}{\partial\boldsymbol{Q}} : \dot{\boldsymbol{Q}} \geq 0. \tag{32}$$

Observe that $\dot{\bar{\boldsymbol{C}}} = (\partial\bar{\boldsymbol{C}}/\partial\boldsymbol{C}) : \dot{\boldsymbol{C}}$ from the chain rule. Then, using

$$\frac{\partial\bar{\boldsymbol{C}}}{\partial\boldsymbol{C}} = J^{-2/3}\left[\mathbb{I} - \frac{1}{3}\boldsymbol{C}\otimes\boldsymbol{C}^{-1}\right] \tag{33}$$

in (32) yields

$$\begin{aligned}&\left\{\boldsymbol{S} : \left[\frac{1}{3}\boldsymbol{C}\frac{1}{\Theta^{\mathrm{e}}}\right] - \frac{\partial\bar{\psi}}{\partial\Theta^{\mathrm{e}}}\right\}\dot{\Theta}^{\mathrm{e}}\\ &\quad + \left\{\boldsymbol{S}\frac{1}{2}\left[\mathbb{I} - \frac{1}{3}\boldsymbol{C}\otimes\boldsymbol{C}^{-1}\right] - \frac{\partial\bar{\psi}}{\partial\boldsymbol{C}} : J^{-2/3}\left[\mathbb{I} - \frac{1}{3}\boldsymbol{C}\otimes\boldsymbol{C}^{-1}\right]\right\} : \dot{\boldsymbol{C}}\\ &\quad + \frac{1}{3}\boldsymbol{S} : \boldsymbol{C}\frac{\dot{\Theta}^{\mathrm{i}}}{\Theta^{\mathrm{i}}} - \frac{\partial\bar{\psi}}{\partial\boldsymbol{Q}} : \dot{\boldsymbol{Q}} \geq 0.\end{aligned} \tag{34}$$

We point out that the derivative in (33) gives rise to the deviatoric projection operator (18) for contravariant tensors in the reference configuration. Using (18) and observing that relation (34) must hold for all possible processes, the argument put forward by Coleman and Noll (see [33]) yields the desired results,

$$\frac{1}{3}\boldsymbol{S} : \boldsymbol{C} = \Theta^{\mathrm{e}}\frac{\partial\bar{\psi}}{\partial\Theta^{\mathrm{e}}}, \tag{35}$$

$$\mathrm{DEV}[\boldsymbol{S}] = 2J^{-2/3}\mathrm{DEV}\left[\frac{\partial\bar{\psi}}{\partial\boldsymbol{C}}\right], \tag{36}$$

and the dissipation rate is nonnegative and given by

$$\frac{1}{3}\boldsymbol{S} : \boldsymbol{C}\frac{\dot{\Theta}^{\mathrm{i}}}{\Theta^{\mathrm{i}}} - \frac{\partial\bar{\psi}}{\partial\boldsymbol{Q}} : \dot{\boldsymbol{Q}} \geq 0. \tag{37}$$

In the present setting, $\boldsymbol{S} : \boldsymbol{C}$ is the trace of the second Piola–Kirchhoff stress tensor. Accordingly, (35) and (36) provide constitutive equations for the pressure, defined as $p_S := \frac{1}{3}\boldsymbol{S} : \boldsymbol{C}$, and deviatoric stress, $\mathrm{DEV}[\boldsymbol{S}]$, respectively. Furthermore, (37) demonstrates that the inelastic volume change ratio, Θ^{i}, is dissipation-conjugate to the pressure, p_S, as might be expected.

Remark 3.1. In keeping with the notion of inelastic deformation, a configuration in which the jacobian is given by $J = \Theta^{\mathrm{i}}$ represents a pressure-free state, unloaded elastically by $\Theta^{\mathrm{e}^{-1}}$.

3.3. Stress Dependence of Diffusivity and Reaction Constant

The notions of stress-dependent diffusivity and reaction constants were introduced in Section 2.1. The specific forms adopted for the dependencies are discussed here. The diffusivity and reaction constant are written as

$$D = D_0 \exp\left(\frac{pV_d}{kT}\right), \quad k_s = k_{s_0} \exp\left(\frac{pV_r}{kT}\right), \tag{38}$$

where D_0 and k_{s_0} are the stress-free diffusivity and reaction constant, respectively, V_d and V_r are the activation volumes corresponding to diffusion and reaction, respectively, k is Boltzmann's constant, and T is temperature in Kelvin, as before. The pressure is p, defined in terms of the trace of the Cauchy stress tensor, $p = 1/3(\boldsymbol{\sigma} : \mathbf{1})$, and is negative in compression.

The stress-dependence of D used here is identical with that proposed in earlier studies on this subject—see Rafferty and co-workers [34], Uchida *et al.* [6], Senez *et al.* [5], and Navi and Dunham [16]. In contrast to these studies, in the present work, the reaction constant is enhanced or depressed by the pressure, p, rather than the normal stress, $\boldsymbol{n} \cdot \boldsymbol{\sigma n}$ ($\boldsymbol{n}$ being normal to the Si-SiO_2 interface. Γ). The justification for this difference follows. Earlier investigations treated the oxide expansion as one-dimensional and modeled it as the movement of the interface normal to itself. The stress opposing this expansion is the (compressive) normal stress, $\boldsymbol{n} \cdot \boldsymbol{\sigma n}$. The extra work to be performed to overcome the energy barrier to reaction is $\boldsymbol{n} \cdot \boldsymbol{\sigma n} V_r$. An Arrhenius law dependence is assumed, leading to the formula $k_s = k_{s_0} \exp(\boldsymbol{n} \cdot \boldsymbol{\sigma n} V_r / kT)$. In contrast, the present study models isotropic expansion of the oxide (see Section 3.2). The stress component that is work-conjugate to volumetric strain is the pressure. Following a line of reasoning identical to that just advanced, the work to be performed in overcoming the energy barrier to reaction is pV_r. Hence, it is this factor, modifying the activation energy, that enhances or depresses the reaction constant.

4. NUMERICAL METHODS

The two preceding sections detailed advances in the mathematical and mechanics formulations. The material in this section focuses on numerical methods. The problem of thermal oxidation of silicon as formulated in this work involves the coupled solution of (i) diffusion-reaction, (ii) level-set evolution, and (iii) mechanics. This section begins with a treatment of advances in numerical methods employed for these distinct problems. The methods are then unified in a staggered solution scheme whose description appears in Section 4.4.

4.1. Numerical Implementation of the Diffusion-Reaction Problem

The weak form of the diffusion-reaction problem is given by (12). At the interface, Γ, the oxidant concentration, ρ, and flux, $\boldsymbol{T}$, can be discontinuous. In the present approach the level-set method is used, by which an interface is allowed to pass through an element. Knowledge of the values of the level-set function (see Section 4.2) enables precise specification of the interface on which ρ^h, the finite-dimensional approximation to ρ, is discontinuous. Rao *et al.* [2] adopt an incompatible modes approach wherein the finite-dimensional concentration

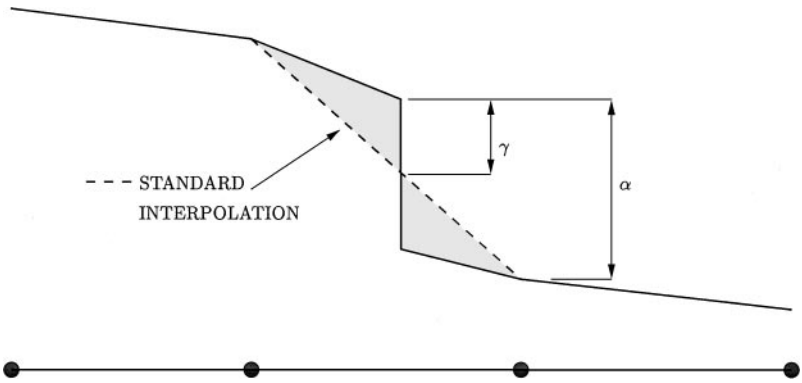

FIG. 3. Incompatible mode interpolation in one dimension.

field is given within an element, e, as

$$\rho_e^h = \underbrace{\sum_{A=1}^{n_{\text{el}}} N^A q^A}_{\text{standard interpolations}} + \underbrace{\tilde{N}\gamma\alpha}_{\text{incompatible mode}} . \tag{39}$$

In (39), N^A denote Lagrange polynomials, n_{el} is the number of element nodes, q^A are nodal values, $\tilde{N}$ is the chosen interpolation function for the incompatible mode, and α is the corresponding degree of freedom. Incompatible mode shape functions, $\tilde{N}$, are chosen that incorporate a discontinuity. The parameter $\gamma \in [0, 1]$ determines the relative magnitudes of the positive and negative contributions from the discontinuity (i.e., the extent to which it adds to or subtracts from the standard interpolation). Figure 3 provides a one-dimensional rendering.

As in other implementations of incompatible mode interpolations (see Fenves *et al.* [35], Taylor *et al.* [36], Simo and Rifai [37] and references in the latter), the corresponding degrees of freedom are statically condensed out. In the present setting, this can be achieved in closed form via the relations

$$[\![\boldsymbol{T} \cdot \boldsymbol{n}]\!]|_\Gamma = -k_s \rho|_{\Gamma^-}, \quad \frac{\rho|_{\Gamma^+}}{\rho_{\Gamma^-}} = m. \tag{40}$$

In (40), $\rho|_{\Gamma^-}$ and $\rho|_{\Gamma^+}$ are concentrations on either side of Γ and m is the so-called concentration segregation constant, which is specified for the problem. The derivation of (40a) is provided in Rao and Hughes [1]. The closed-form static condensation procedure is described in Rao *et al.* [2]. In closing this subsection attention is also called to an application of partition of unity finite-element methods for modeling the displacement field around cracks by Moës and co-workers [38], which bears relation to the incompatible modes' method described here.

4.1.1. *A Penalty Formulation to Ensure Positive Concentrations*

In certain situations, the incompatible mode interpolations have been observed to result in negative concentrations at nodes downstream (with respect to interface velocity) of Γ.

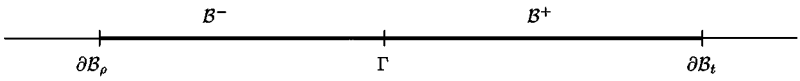

FIG. 4. Domain, boundaries, and interface for the one-dimensional diffusion problem.

Clearly, this is nonphysical. Recourse has therefore been taken in this work to a penalty formulation to ensure positive nodal concentrations. The approach is described below.

Consider adding to the specification of the problem outlined above an inhomogeneous diffusivity $D(\boldsymbol{x})$:

$$D(\boldsymbol{x}) = \begin{cases} D^-: & \boldsymbol{x} \in \Omega^- \\ D^+: & \boldsymbol{x} \in \Omega^+. \end{cases} \tag{41}$$

Then, for the one-dimensional steady-state diffusion problem over $\mathcal{B} \subset \mathbb{R}$ (Fig. 4), written in strong form,

$$\text{find} \quad \rho \in \mathcal{S} = \{\rho \in \mathrm{L}_2(\mathcal{B}) \mid \rho = \rho_g \text{ on } \partial\mathcal{B}_\rho\} \tag{42}$$

$$\text{and} \quad T = -D(x)\frac{\mathrm{d}\rho}{\mathrm{d}x} \quad \text{in } \mathcal{B}\backslash\Gamma, \quad T = 0 \quad \text{on } \partial\mathcal{B}_t, \tag{43}$$

$$\text{such that} \quad \frac{\mathrm{d}}{\mathrm{d}x}T(x) = 0 \quad \text{in } \mathcal{B}\backslash\Gamma, \tag{44}$$

$$[\![T]\!]|_\Gamma = -k_s\rho|_{\Gamma^-}, \quad \frac{\rho|_{\Gamma^+}}{\rho|_{\Gamma^-}} = m. \tag{45}$$

With $\partial\mathcal{B}_\rho$, $\partial\mathcal{B}_t$, and Γ now being points in $\mathbb{R}$ and with $\partial\mathcal{B}_\rho$ lying to the left of $\partial\mathcal{B}_t$, the concentration in $\mathcal{B}^+$ is constant and given by

$$\bar{\rho} = \frac{mD^-\rho_g}{D^- - k_s h^-}. \tag{46}$$

In the above expression, $h^- = m(\mathcal{B}^-)$ is the length of $\mathcal{B}^-$. In the convention adopted for this work, the reaction constant k_s is a negative number; accordingly, $\bar{\rho}$ is always nonnegative. It is this property of the one-dimensional solution that we seek to enforce on the multidimensional problem in its discrete form.

A quadratic penalty function is constructed:

$$\chi(\rho_g, \bar{\rho}) := \frac{1}{2}K\left(\frac{mD^-\rho_g}{D^- - k_s h^-} - \bar{\rho}\right)^2. \tag{47}$$

Here, K is the penalty parameter, and ρ_g and $\bar{\rho}$ are the concentrations at suitably chosen points $\boldsymbol{x}_g \in \Omega^-$ and $\bar{\boldsymbol{x}} \in \Omega^+$, respectively. The length parameter h^- is the distance of point $\boldsymbol{x}_g$ from Γ.

The modification to the weak form is obtained by considering variations $\rho_g + \varepsilon w_g$ and $\bar{\rho} + \varepsilon\bar{w}$ and finding the stationary point of the penalty function:

$$\begin{aligned} &\frac{\mathrm{d}}{\mathrm{d}\varepsilon}\left\{\frac{1}{2}K\left(\frac{mD^-(\rho_g + \varepsilon w_g)}{D^- - k_s h^-} - (\bar{\rho} + \varepsilon\bar{w})\right)^2\right\}\Bigg|_{\varepsilon=0} = 0, \\ &\Rightarrow \left(\frac{mD^- w_g}{D^- - k_s h^-} - \bar{w}\right)K\left(\frac{mD^-\rho_g}{D^- - k_s h^-} - \bar{\rho}\right) = 0. \end{aligned} \tag{48}$$

The above procedure can be generalized by starting with a penalty function $\chi(\boldsymbol{\rho}_g, \bar{\boldsymbol{\rho}})$ (using the same symbol, χ, in an abuse of notation) defined for vectors $\boldsymbol{\rho}_g = \langle \rho_{g_1}, \rho_{g_2}, \ldots, \rho_{g_p} \rangle^T$, $\bar{\boldsymbol{\rho}} = \langle \bar{\rho}_1, \bar{\rho}_2, \ldots, \bar{\rho}_p \rangle^T$ as

$$\chi(\boldsymbol{\rho}_g, \bar{\boldsymbol{\rho}}) = \sum_{i=1}^{p} \frac{1}{2} K_i \left(\frac{m D^- \rho_{g_i}}{D^- - k_s h_i^-} - \bar{\rho}_i \right)^2. \tag{49}$$

In the present setting, the penalty function in (49) can be regarded as enforcing the desired constraint between each pair in the set $\{(\rho_{g_1}, \bar{\rho}_1), (\rho_{g_2}, \bar{\rho}_2), \ldots, (\rho_{g_p}, \bar{\rho}_p)\}$. The condition for the stationary point of this extended penalty function is

$$\sum_{i=1}^{p} \left(\frac{m D^- w_{g_i}}{D^- - k_s h_i^-} - \bar{w}_i \right) K_i \left(\frac{m D^- \rho_{g_i}}{D^- - k_s h_i^-} - \bar{\rho}_i \right) = 0. \tag{50}$$

Equation (50) is added to (12) to yield the penalized weak form

$$\int_{\Omega \setminus \Gamma} \nabla w \cdot \boldsymbol{T} \, dV - \int_{\Gamma} w [\![\boldsymbol{T} \cdot \boldsymbol{n}]\!] \, ds + \sum_{i=1}^{i=p} \left(\frac{m D^- w_{g_i}}{D^- - k_s h_i^-} - \bar{w}_i \right) K_i \left(\frac{m D^- \rho_{g_i}}{D^- - k_s h_i^-} - \bar{\rho}_i \right)$$
$$= - \int_{\Omega} f \, dV + \int_{\partial \Omega_t} t \, ds. \tag{51}$$

Consider the set $N_{\Gamma_t} = \{ n_e \mid \Gamma_t \cap \Omega_{n_e} \neq \emptyset \}$ containing the numbers of those elements which are intersected by Γ_t. The points $\boldsymbol{x}_{g_i}$ and $\bar{\boldsymbol{x}}_i$ (with concentrations ρ_{g_i} and $\bar{\rho}_i$) are most conveniently chosen to each lie in an element $e \in N_\Gamma$. The finite-dimensional version of (51) is simply written as

$$\int_{\Omega \setminus \Gamma} \nabla w^h \cdot \boldsymbol{T}^h \, dV - \int_{\Gamma} w^h [\![\boldsymbol{T}^h \cdot \boldsymbol{n}]\!] \, ds + \sum_{e \in N_\Gamma} \left(\frac{m D^- w^h_{g_e}}{D^- - k_s h_e^-} - \bar{w}^h_e \right)$$
$$\times K_e \left(\frac{m D^- \rho^h_{g_e}}{D^- - k_s h_e^-} - \bar{\rho}^h_e \right) = \int_{\Omega} w^h f \, dV + \int_{\partial \Omega_h} w^h \bar{h} \, ds. \tag{52}$$

In (52), K_e are penalty parameters which are free to be chosen differently for each element. The choice of points $\boldsymbol{x}_{g_e}$ and $\bar{\boldsymbol{x}}_e$ is best explained using Fig. 5 for the two possible configurations which depend on the orientation of a triangular element with respect to $\boldsymbol{n}$.

The cases depicted correspond to situations in which the isolated node, i, lies in Ω^- (Fig. 5a) and conversely (Fig. 5b). In Fig. 5a, $x_{g_e} = x^i$ and $\rho^h_g = q^i$, $\bar{\boldsymbol{x}}_e = (\boldsymbol{x}^j + \boldsymbol{x}^k)/2$,

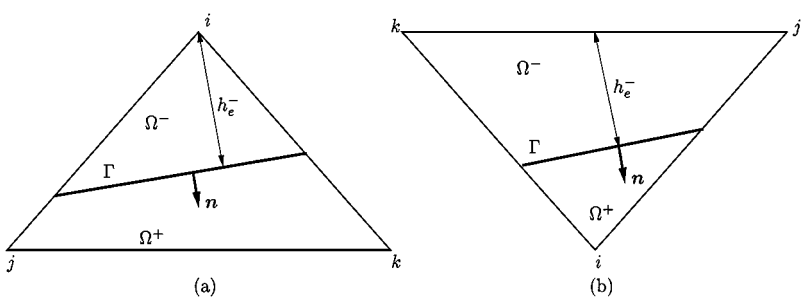

FIG. 5. Possible orientations of the triangle with respect to $\boldsymbol{n}$.

and $\bar{\rho}^h = (q^j + q^k)/2$, where the qs are nodal concentration values. In Fig. 5b, $\boldsymbol{x}_{g_e} = (\boldsymbol{x}^j + \boldsymbol{x}^k)/2$ and $\rho_g^h = (q^j + q^k)/2$, $\bar{\boldsymbol{x}}_e = \boldsymbol{x}^i$, and $\bar{\rho}^h = q^i$. The same rule is applied in selecting the weighting function values w_g^h and $\bar{w}^h$.

The penalty formulation presented above is found to be effective in preventing negative concentration values. Numerical examples are provided in Section 5.

4.2. Algorithmic Implementation of the Level-Set Formulation

The level-set equation (5) is cast in weak form as follows. Find $\phi(\boldsymbol{x}, t) \in H^1(\Omega)$ such that $\forall\, \vartheta(\boldsymbol{x}) \in H^1(\Omega)$, and $\phi(\boldsymbol{x}, 0) = \phi_0(\boldsymbol{x})$,

$$\int_\Omega \vartheta \frac{\partial \phi}{\partial t}\, dV + \int_\Omega \vartheta\, v^N \|\nabla \phi\|\, dV = 0, \tag{53}$$

where ϑ is the weighting function. On discretizing, for instance, using linear finite-element interpolations and a semidiscrete time integration scheme, the matrix problem that results is

$$\boldsymbol{M}(\phi_{n+1} - \phi_n) + \Delta t\, \mathcal{R}^h_{n+\alpha} = 0, \tag{54}$$

$$\phi(0) = \phi_0, \tag{55}$$

where ϕ is the vector of nodal values of ϕ, $\boldsymbol{M}$ is the finite-element mass matrix, $(\bullet)_n$ denotes the algorithmic approximation to the corresponding quantity at the time instant t_n, Δt is the time increment, and the static residual $\mathcal{R}^h$ arises from the second integral in (53). The generalized midpoint family of algorithms is implied in the numerical integration formula of (54), and $\alpha \in [0, 1]$. As usual, the superscript $(\bullet)^h$ indicates that the corresponding quantities are arrived at via a finite-dimensional approximation. Observe that the static residual is a nonlinear function of ϕ^h. In general, this requires the application of an iterative procedure for the solution of (55). However, a particularly simple form results by selecting the forward Euler algorithm ($\alpha = 0$). Recalling that for the solution at time t_{n+1}, this algorithm involves the evaluation of $\mathcal{R}^h$ at t_n, it follows that v_n^N and $\|\nabla \phi_n\|$ must be used in (53). With a diagonalized mass matrix, this algorithm is an especially fast scheme, since neither does the mass matrix $\boldsymbol{M}$ need inversion nor is an iterative scheme implemented. Stability restrictions do impose an upper bound on Δt, as is well-known.

The velocity projection scheme introduced in Section 2.2 provides the interface velocity in elements not containing Γ. In Fig. 6, n is such an element. The algorithm for determining the normal velocity is based upon a dynamically updated set $N_{\Gamma_{n+1}}$ ($n+1$ is the discrete representation of the subscript t, for time), as follows.

Time t_{n+1}, element m, quadrature point $\boldsymbol{y}_k$
IF $(\phi^h_{n+1}(\boldsymbol{y}_k) = 0)$ THEN $(m \in N_{\Gamma_{n+1}})$
$\quad v^N = -\frac{[\![\boldsymbol{T}_{ox} \cdot \boldsymbol{n}]\!]}{[\![\rho_{ox}]\!]}$
ELSE $(m \notin N_{\Gamma_{n+1}})$
1. Find $\boldsymbol{x}_L$ (quadrature point of n_e) such that
$\quad \|\boldsymbol{x}_L - \boldsymbol{y}_k\| = \min_{n_e \in N_{\Gamma_{n+1}}} \min_{l \in \{1,\ldots,l_{\text{int}}\}} \|\boldsymbol{x}_l - \boldsymbol{y}_k\|$
2. Set $v^N|_{m,\boldsymbol{y}_k} = v^N|_{n_e,\boldsymbol{x}_L}$
ENDIF

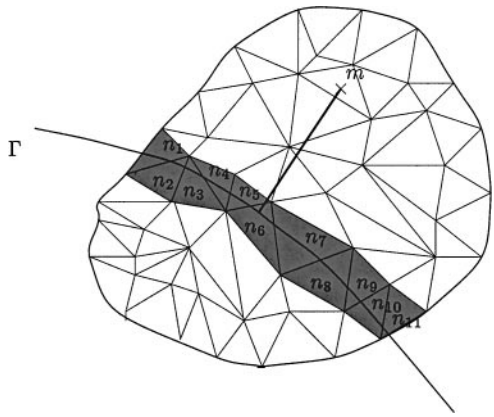

FIG. 6. Velocity projection scheme for element $\boldsymbol{n}$ using the set of elements N_Γ (shaded elements).

In practice, the use of linear finite-element interpolations requires a single quadrature point in each element, simplifying and speeding up the algorithm. Within each element, the above search is of $\mathcal{O}(m[N_\Gamma])$, where $m[N_\Gamma]$ is the number of elements in N_Γ.

4.2.1. *Spatial Stabilization*

The level-set formalism yields a nonlinear advection equation which demonstrates spatial oscillations since the element Peclet number is infinite in the absence of a diffusive term. The Galerkin least squares approach of Hughes and co-workers [39–43] has been employed by Rao *et al.* [2] to stabilize this equation. This involves the modification of the weak form (53) to yield a stabilized weak form:

$$\int_\Omega \vartheta \frac{\partial \phi}{\partial t}\,\mathrm{d}V + \int_\Omega \vartheta v^N \|\nabla\phi\|\,\mathrm{d}V + \underbrace{\tau \int_\Omega v^N \frac{\nabla\phi}{\|\nabla\phi\|}\nabla\vartheta\left(\frac{\partial\phi}{\partial t} + v^N\|\nabla\phi\|\right)\mathrm{d}V}_{\text{stabilizing term}} = 0. \quad (56)$$

The parameter τ is the so-called stabilization parameter whose choice is not a trivial task. The success of stabilization schemes of this form hinges on the value used for τ. Rao *et al.* [2] base their calculation of τ upon the analysis in Hughes *et al.* [42]. However, this choice fails to eliminate oscillations in the solution for certain extreme cases. For the present work the choice of τ is based upon the work of Brezzi and Russo [44] and Hughes [45] and produces oscillation-free behavior for the range of problems considered.

The level-set method has been applied to track-moving interfaces in a number of situations. For a recent application also involving a combination of the level-set method with finite element techniques for crack propagation, see the work of Stolarska and co-workers [46].

4.3. Enhanced Strain Formulation for Inhomogeneous Expansion

The computational efficiency afforded by level-set methods requires the enrichment of interpolation techniques at the element-level. This has been described in the context of the diffusion-reaction problem in Section 4.1. Similarly, the intersection of an element by the interface requires special considerations with regard to numerical implementation of the mechanics of the problem. The interface, Γ, introduces material inhomogeneity at the

element-level by separating the element into Si and SiO_2 parts. Recall (Section 3.2) that the SiO_2-part of such an element undergoes an instantaneous inelastic volume expansion, $\Theta^{\mathrm{i}}_{\mathrm{ox}}$, and one at a finite rate, $\Theta^{\mathrm{i}}_{\mathrm{a}}$. The part of the element that is silicon, however, has a purely elastic volume expansion. The kinematic basis of the element therefore needs enrichment to accurately represent this inhomogeneous expansion. In the present work, the enhanced strain method pioneered by Simo and co-workers [37, 47, 48] (see Glaser & Armero [49] for recent results) has been adopted for this purpose. The use of this framework to describe strongly inhomogeneous strains is based upon the approach in Armero & Garikipati [50].

An enhanced deformation gradient is introduced as follows:

$$\boldsymbol{F} = \underbrace{\frac{\partial \varphi}{\partial \boldsymbol{X}}}_{\hat{\boldsymbol{F}}} + \underbrace{\tilde{\boldsymbol{H}}}_{\text{enhancement}} . \tag{57}$$

The standard definition for the deformation gradient is the first term on the right-hand side in (57), which is now rewritten to distinguish it from the corresponding enhanced quantity, $\boldsymbol{F}$. The second term, $\tilde{H}$, is the enhancement to the standard displacement gradient, $\partial \boldsymbol{u}/\partial \boldsymbol{X}$, introduced in (14b). The above additive decomposition leads to a multiplicative decomposition of the deformation gradient, written as

$$\boldsymbol{F} = \underbrace{(\boldsymbol{1} + \tilde{\boldsymbol{H}}\hat{\boldsymbol{F}}^{-1})}_{\tilde{\boldsymbol{f}}}\hat{\boldsymbol{F}}. \tag{58}$$

In the theory of enhanced strain methods, the above decomposition is introduced by way of a three-field Hu–Washizu variational formulation. The fields $\boldsymbol{u}$, $\tilde{\boldsymbol{H}}$, and $\boldsymbol{P}$ (the nominal stress tensor introduced in Section 3.1) are each defined on $\bar{\Omega} \subset \mathbb{R}^3$ and belong to spaces

$$\boldsymbol{u} \in U := \{\boldsymbol{u} : \bar{\Omega} \mapsto \mathbb{R}^3 \mid \boldsymbol{u} \in H^1(\Omega), \quad \boldsymbol{u} = \boldsymbol{u}_g \text{ on } \partial\Omega_u\}, \tag{59}$$

$$\tilde{\boldsymbol{H}},\ \boldsymbol{P} \in L := \{\boldsymbol{A} : \bar{\Omega} \mapsto \mathbb{GL}(3) \mid \boldsymbol{A} \in L^2(\Omega)\}, \tag{60}$$

where $\mathbb{GL}(3)$ is the space of 3×3 matrices introduced in Section 3.1. A suitably defined potential energy functional is introduced, $\Pi : U \times L \times L \mapsto \mathbb{R}$, whose stationary point is found with respect to variations ($\delta\boldsymbol{u}$, $\delta\tilde{\boldsymbol{H}}$, $\delta\boldsymbol{P}$). Standard calculus of variations, supplemented by the requirement that $\tilde{\boldsymbol{H}}$ be L^2-orthogonal to $\boldsymbol{P}$, give rise to the following pair of equations, which constitute the weak form corresponding to the enhanced strain method:

$$\int_\Omega \mathrm{Grad}[\delta\boldsymbol{u}] : \boldsymbol{P}\, dV = \int_\Omega \delta\boldsymbol{u} \cdot \boldsymbol{f}\, dV + \int_{\partial\Omega_t} \delta\boldsymbol{u} \cdot \boldsymbol{t}\, dS, \tag{61a}$$

$$\int_\Omega \delta\tilde{\boldsymbol{H}} : \boldsymbol{P}\, dV = 0. \tag{61b}$$

Additionally, in a finite-element setting, the relatively weak requirement that the enhanced displacement gradient, $\tilde{\boldsymbol{H}}$, and nominal stress, $\boldsymbol{P}$, lie in $L^2(\Omega)$ allows $\tilde{\boldsymbol{H}}^h$ to be defined discontinuously across element boundaries. Then, (61b) can be written [now using finite-dimensional fields denoted $(\bullet)^h$] as

$$\sum_{e=1}^{n_{\mathrm{el}}} \int_{\Omega_e} \delta\tilde{\boldsymbol{H}}^h : \boldsymbol{P}^h\, dV = 0. \tag{62}$$

Equation (62) allows the local elimination of $\tilde{\boldsymbol{H}}$ via static condensation.

Equation (62) also gives rise to a consistency condition on imposing the requirement that the method be capable of representing stress fields that are constant over Ω_e. The condition is posed in terms of the volume integral of $\delta\tilde{\boldsymbol{H}}$ over Ω_e:

$$\int_{\Omega_e} \delta\tilde{\boldsymbol{H}}^h \, dV = 0. \tag{63}$$

In discrete form, $\tilde{\boldsymbol{H}}$ and $\delta\tilde{\boldsymbol{H}}$ are expressed as local, element-level interpolations of scalar parameters, β and ζ, respectively.

$$\tilde{\boldsymbol{H}}^h(\boldsymbol{X}) = \beta \boldsymbol{G}(\boldsymbol{X}), \quad \delta\tilde{\boldsymbol{H}}^h(\boldsymbol{X}) = \zeta \boldsymbol{G}(\boldsymbol{X}), \tag{64}$$

where $\boldsymbol{G}(\boldsymbol{X})$ is a suitably defined interpolation function. Substituting (64) in (63) leads to

$$\int_{\Omega_e} \boldsymbol{G}(\boldsymbol{X}) \, dV = 0. \tag{65}$$

Simo and Armero [47] observe that (63) is closely related to satisfaction of the classical patch test of Taylor *et al.* [51]. In the case being pursued here, the construction of $\boldsymbol{G}(\boldsymbol{X})$ is based upon the idea that the corresponding enhancement to the deformation gradient, $\tilde{\boldsymbol{f}}^h = \boldsymbol{1} + \tilde{\boldsymbol{H}}\hat{\boldsymbol{F}}^{h-1} = \boldsymbol{1} + \beta \boldsymbol{G}\hat{\boldsymbol{F}}^{h-1}$ [see (58)], must be isotropic. Further, $\boldsymbol{u}^h$ is interpolated linearly over Ω_e, rendering $\hat{\boldsymbol{F}}^h$ a constant, and $\boldsymbol{G}(\boldsymbol{X})$ is chosen to be piecewise constant in Ω_e^- and Ω_e^+. This allows $\boldsymbol{G}(\boldsymbol{X})$ to be written as

$$\boldsymbol{G}(\boldsymbol{X}) = \begin{cases} \frac{1}{l^-}\hat{\boldsymbol{F}}^h: & \boldsymbol{X} \in \Omega_e^- \\ \frac{1}{l^+}\hat{\boldsymbol{F}}^h: & \boldsymbol{X} \in \Omega_e^+ \end{cases}, \tag{66}$$

where one of the lengths l^-, l^+ must be arbitrarily chosen. Equation (65) leads to the relation

$$l^+ = -l^- \frac{m(\Omega_e^+)}{m(\Omega_e^-)}. \tag{67}$$

Finally, l^- is arbitrarily chosen equal to the element diameter h_e.

Remark 4.2. On recalling the volumetric-deviatoric decomposition on $\boldsymbol{F}$ in Sections 3.1 and 3.2, it is clear that the enhancement introduced in (58) is easily incorporated in the framework of the previous sections. In particular, the following relations hold:

$$\hat{\boldsymbol{F}} = (\det[\hat{\boldsymbol{F}}])^{1/3}\bar{\boldsymbol{F}}, \quad \tilde{\boldsymbol{f}} = (\det[\,\tilde{\boldsymbol{f}}\,])^{1/3}\boldsymbol{1}, \tag{68}$$

$$J = \Theta = \Theta^e\Theta^i = \det[\,\tilde{\boldsymbol{f}}\,]\det[\hat{\boldsymbol{F}}]. \tag{69}$$

Section 5 contains numerical examples that demonstrate the good performance of this rendering of the enhanced strain method in resolving highly inhomogeneous volume strains.

4.4. Staggered Solution of Coupled Problems

The methods described above are combined in the following staggered algorithm:

At time t_{n+1}, given the solution at t_n (i.e., $\{\rho_n, \boldsymbol{T}_n, \phi_n, v_n^N, \boldsymbol{u}_n, \boldsymbol{F}_n, \Theta^{\mathrm{i}}_{\mathrm{ox},n}, \Theta^{\mathrm{i}}_{\mathrm{a},n}, \boldsymbol{Q}_n, \boldsymbol{\sigma}_n\}$ are known).

1. Determine Si and SiO_2 regions on the basis of ϕ_n.
2. Solve the diffusion-reaction problem (52) using $\boldsymbol{\sigma}_n$ to calculate stress-dependent $D^{\pm}$ and k_s to give ρ_{n+1} and T_{n+1} in $\Omega\backslash\Gamma$ and hence calculate v_{n+1}^N employing the velocity projection algorithm described in Section 4.2.
3. With v_n^N, solve the level-set evolution problem employing the methods described in Section 4.2 to obtain ϕ_{n+1}.
4. Determine Si and SiO_2 regions on the basis of ϕ_{n+1}.
5. Solve the mechanics problem employing constitutive integration rules in (20), (26), and (28a) to obtain $\boldsymbol{u}_{n+1}, \boldsymbol{F}_{n+1}, \Theta^{\mathrm{i}}_{\mathrm{ox},n+1}, \Theta^{\mathrm{i}}_{\mathrm{a},n+1}, \boldsymbol{Q}_{n+1}, \boldsymbol{\sigma}_{n+1}$.
6. Set $t_n = t_{n+1}$, $t_{n+1} = t_{n+1} + \Delta t$. Go to 1.

The definitions of Si and SiO_2 regions for the diffusion-reaction problem are based upon ϕ_n and are unchanged over the time step $[t_n, t_{n+1}]$. The stress-dependence of D and k_s for the diffusion-reaction problem are determined from σ_n. Accordingly, these values are constant over $[t_n, t_{n+1}]$. It follows that the solution of the diffusion-reaction problem is obtained with a single iteration for the time step. With the forward Euler algorithm, the solution of the level-set problem is entirely dependent on the interface normal velocity, v_n^N, determined at the end of the previous time step, t_n. Thus, the definition of Si and SiO_2 regions as determined by solving the level-set problem over the current time step $[t_n, t_{n+1}]$ is obtained with a single iteration. Finally, the solution of the mechanics problem is nonlinear and uses ϕ_{n+1} (updated by the most recent solution of the level-set equation) to determine silicon and SiO_2 regions. On the basis of these updates, it is clear that a second pass through steps 1–5 leaves the solution of each problem unchanged. It follows that the above staggered scheme converges in a single pass.

5. NUMERICAL EXAMPLES

The models developed in preceding sections are demonstrated by way of numerical examples applied to a range of intial and boundary value problems. Modeling advances pertaining to a particular phenomenon (i.e., diffusion-reaction), the level-set formulation, and mechanics are first presented in isolation on simple academic problems. Finally they are combined in the numerical solution of a process sequence in semiconductor manufacture.

5.1. Penalty Formulation of Discontinuous Concentration

5.1.1. *One-Dimensional Diffusion-Reaction*

We first consider an effectively one-dimensional diffusion-reaction problem incorporating a discontinuity at the Si-SiO_2 interface. The problem domain and boundary conditions appear in Fig. 7. The diffusion-reaction problem is decoupled from mechanics in this

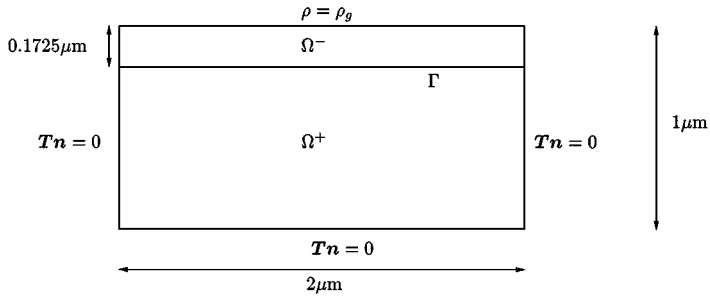

FIG. 7. Problem definition for one-dimensional diffusion-reaction; $\rho_g = 5 \times 10^{16}$ cm^{-3}.

example. The position of the interface, Γ, is also taken to be fixed (i.e., the level set does not evolve). Accordingly, a linear, time-independent problem is to be solved. Material properties and temperature appear in Table I.

Figure 8 shows the concentration field obtained. The sharp contours correspond to the position of the interface and result from smoothing of a discontinuous field in the contour plot. The actual field is discontinuous and the discontinuity lies within the fourth row of elements from the upper surface. The solution obtained agrees with the exact solution outlined in Section 4.1.1 (Eq. 46). In this case the penalty formulation was not employed. The incompatible mode formulation for discontinuous concentration reproduces the exact solution in this one-dimensional setting.

5.1.2. *Diffusion-Reaction Incorporating the Penalty Formulation*

The need for a method enforcing positive concentration and the effectiveness of the proposed penalty formulation is demonstrated in this subsection. The domain and boundary conditions appear in Fig. 9. The presence of a sharp corner in the interface appears to induce negative concentrations in the solution.

As with the previous problem, diffusion-reaction was treated and decoupled from the mechanics and interface motion. Material properties used and the temperature were identical to the one-dimensional boundary value problem. Figure 10 shows the position of the interface on the finite-element mesh. Figures 11 and 12 show the results obtained without and with the penalty formulation, respectively. The nonphysical negative concentration in Ω^+ near the interface corner seen in Fig. 11 does not appear when a penalty parameter $K = 10^3$ (dimensions of s^{-1} is used (see Section 4.1.1).

TABLE I
Properties for One-Dimensional Diffusion-Reaction

Property	Value
$D_{0_{ox}}$	5.0234×10^{-7} cm^2/s
$D_{0_{Si}}$	5.0234×10^{-9} cm^2/s
k_{s_0}	-4.5391×10^{-3} cm/s
T	1323 K

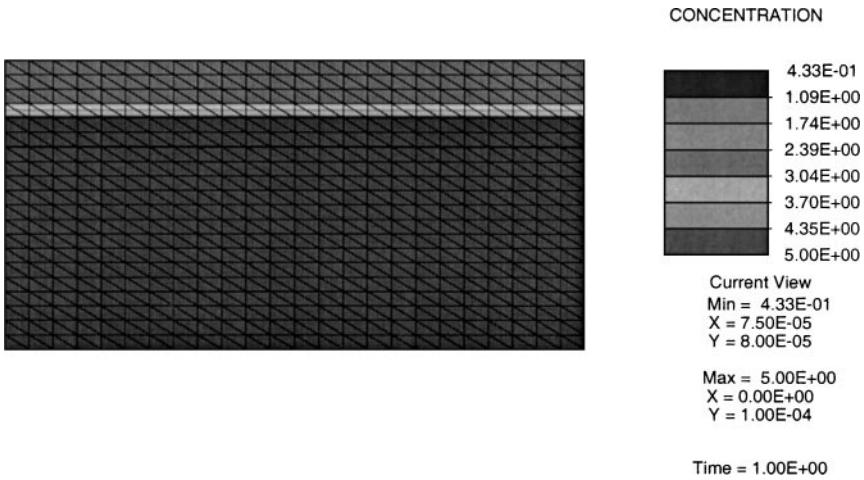

FIG. 8. Contours of oxidant concentration ($\times 10^{16}$ cm^{-3}) showing a discontinuity at Γ.

5.2. Interface Evolution with Velocity Projection and Stabilization

The next pair of examples demonstrate the working of the velocity projection algorithm and the effect of the stabilization parameter used for this work.

The example of Section 5.1.2 is rerun with interface evolution (i.e., the level-set evolution equation is also solved). However, the mechanical problem is still left out. The diffusion-reaction and level-set problems are solved in a staggered fashion (see Section 4.4). Figure 13 shows the initial position of the interface.

Figures 14 and 15 correspond to time instants $t = 480$ s and $t = 1200$ s, respectively. Observe the uniform spacing of level-set contours. The velocity projection scheme works

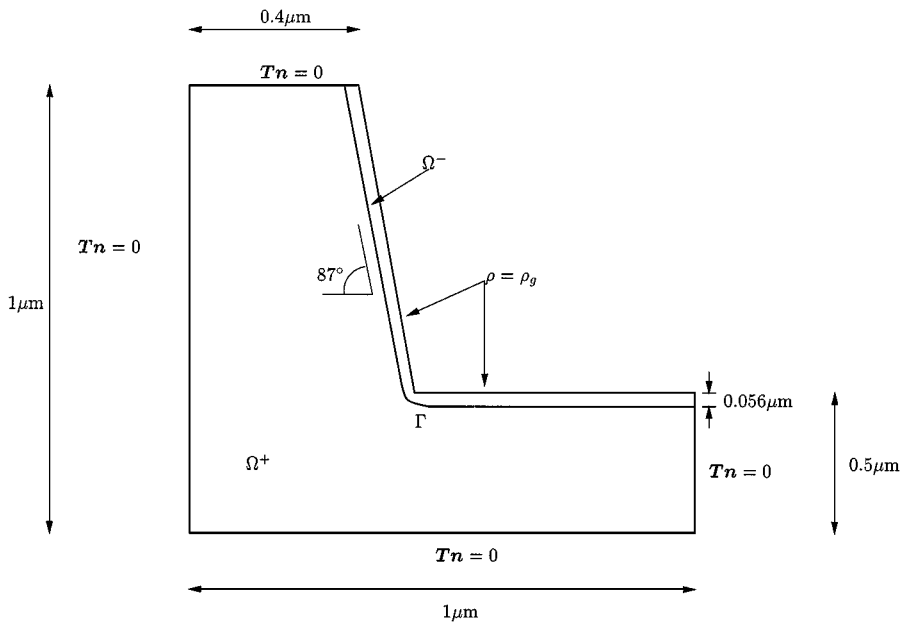

FIG. 9. Problem definition for diffusion-reaction incorporating a corner; $\rho_g = 5 \times 10^{16}$ cm^{-3}.

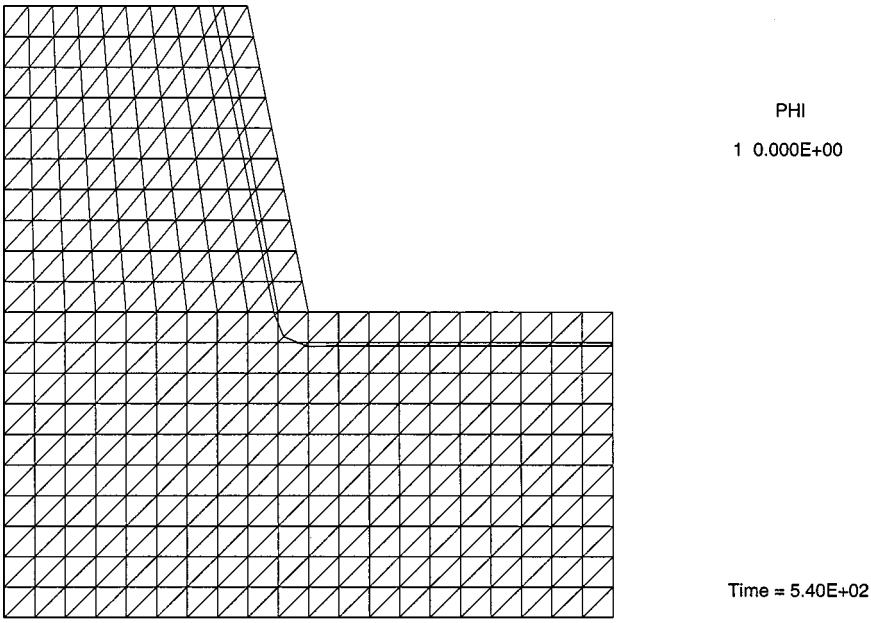

FIG. 10. Location of the interface, Γ.

to ensure that at all points on a given line perpendicular to Γ_t, the level-set contours have the same normal velocity.

It is worth observing that the level-set field is smooth and devoid of oscillations with the chosen stabilization (Section 4.2.1).

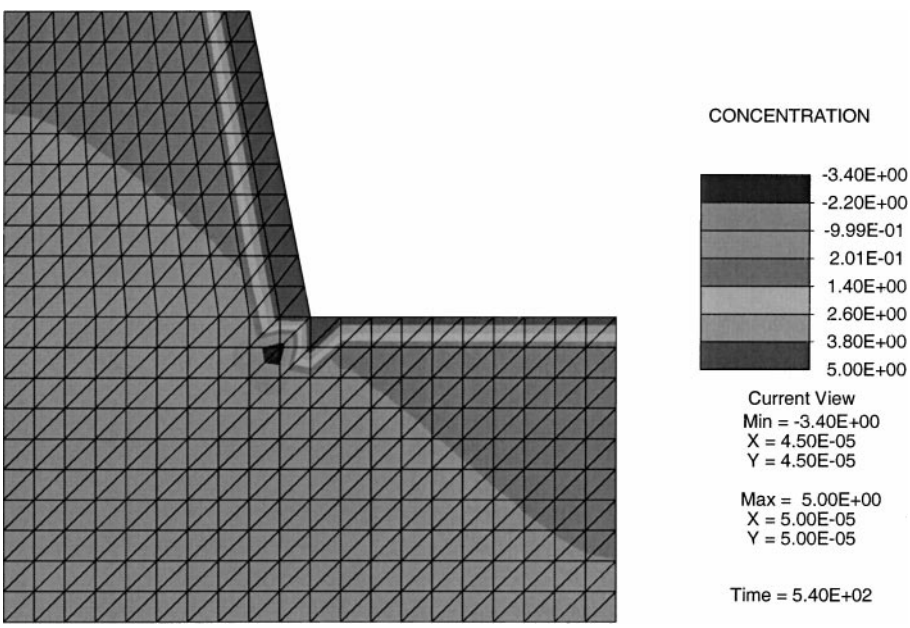

FIG. 11. Appearance of negative concentration (contours are values $\times 10^{16}$ cm^{-3}) at the interface corner.

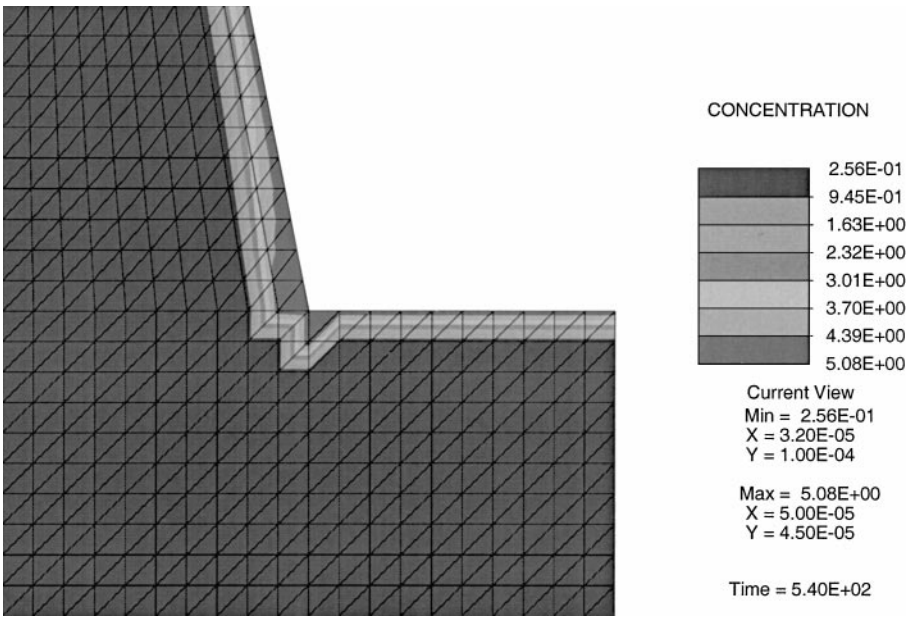

FIG. 12. Concentration remains positive with penalty formulation (contours are values $\times 10^{16}$ cm^{-3}).

5.3. Two-Element Test for Inhomogeneous Expansion

This example demonstrates the enhanced strain formulation for inhomogeneous expansion. An initially square domain is chosen. Figure 16 depicts the problem domain. In this case, the mechanical problem alone needs to be considered. The position of Γ is given and

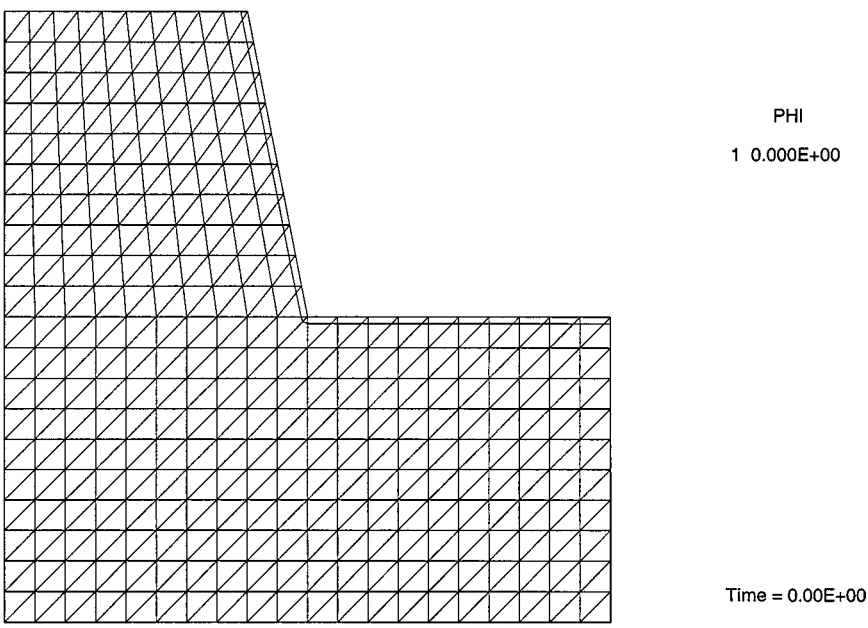

FIG. 13. Initial position of the interface, Γ_0.

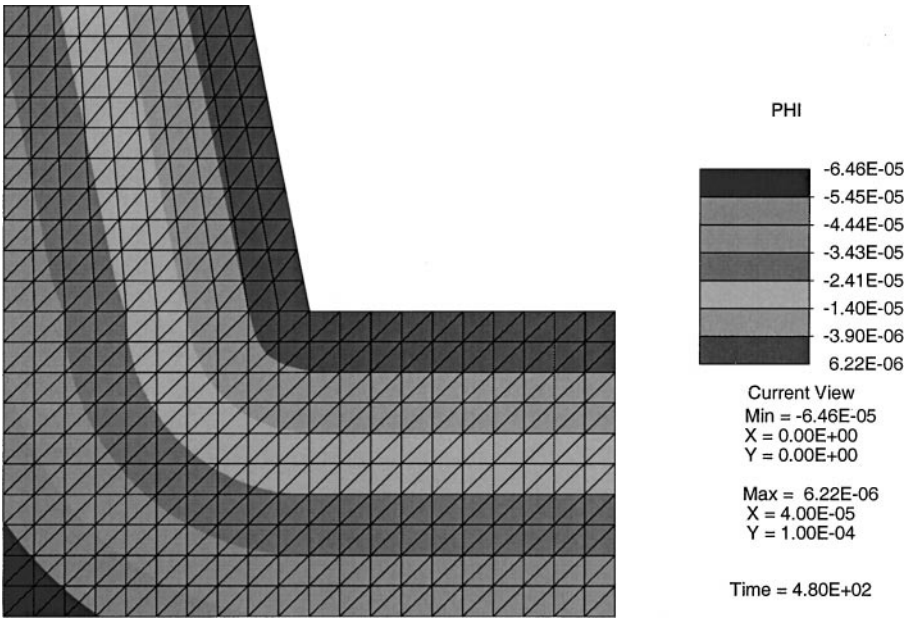

FIG. 14. Level-set contours, ϕ, at $t = 480$ s. The zero level-set contour is not explicitly shown, but its position can be interpolated and lies in the first band from the trench wall.

it separates the domain into Ω^- (SiO_2) and Ω^+ (Si). It is assumed that at time $t = 0^-$, the interface lay outside the domain shown. It follows that with the appearance of Γ in the position shown in Fig. 16, points in Ω^- experience an instantaneous expansion $\Theta^{\mathrm{i}}_{\mathrm{ox}} = 2.2$. The compressible Neo–Hookean stored energy function (Section 3.1) is employed for both

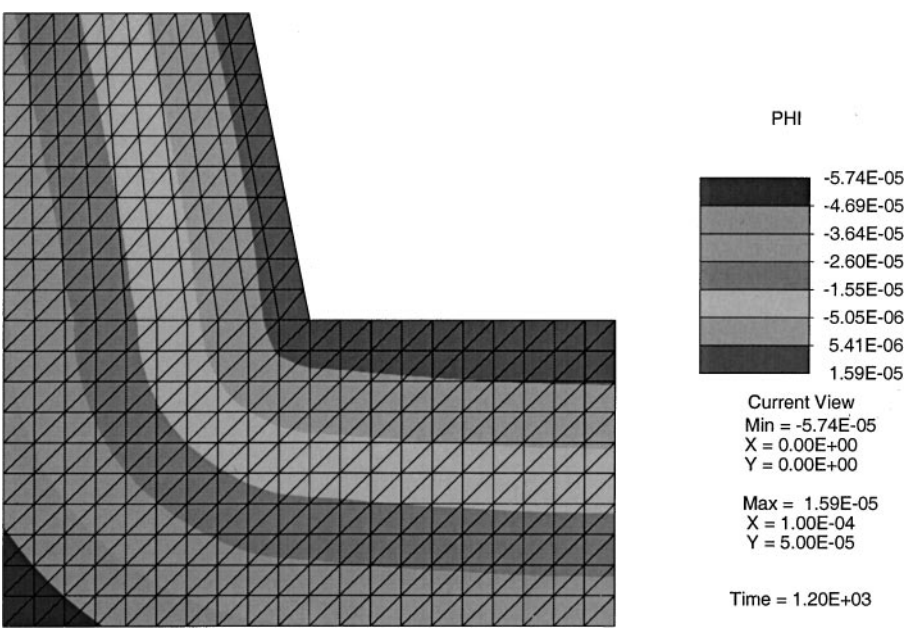

FIG. 15. Level-set contours, ϕ, at $t = 1200$ s. The zero level-set contour is not explicitly shown, but its position can be interpolated and lies in the second band from the trench wall.

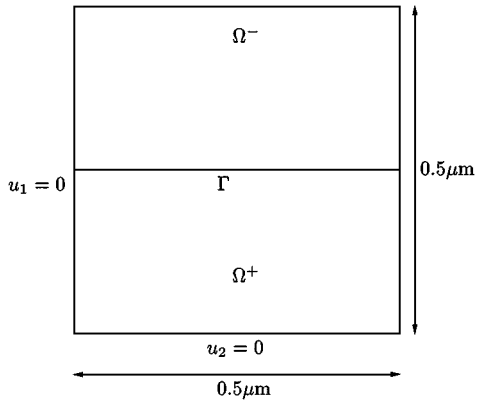

FIG. 16. Domain with inhomogeneous materials: Ω^- : SiO_2, Ω^+ : Si.

Si and SiO_2. In the case of SiO_2, the stored energy function is modified, as discussed in Section 3.1, to incorporate the standard solid viscoelastic model. The relevant material properties and problem parameters appear in Table II. A relatively low temperature is chosen at which SiO_2 does not demonstrate significant viscoelastic behavior (i.e., it can be treated as a purely hyperelastic material) (see Garikipati *et al.* [24]). Additionally, at this temperature the rate of inelastic volume expansion, $\dot{\Theta}^{\mathrm{i}}_{\mathrm{a}}$, is negligible. Hence we have, $\Theta^{\mathrm{i}} \approx \Theta^{\mathrm{i}}_{\mathrm{ox}}$.

A mesh composed of two triangular elements is used. Figures 17 and 18 show the initial ($t = 0^-$) and final ($t = 0^+$) configurations. The large strains involved are apparent. The enhanced strain formulation discussed in Section 4.3 works well in resolving the significantly differing volume strains in Ω_e^- and Ω_e^+ for each element ($e = 1,\ 2$). The total and inelastic volume strains in each subdomain of the elements are listed in Table III.

Next, in order to demonstrate the gradual inelastic volume change during annealing, the above problem is run at a higher temperature, $T = 1323$ K. At this temperature, the rate $\Theta^{\mathrm{i}}_{\mathrm{a}}$ is significant [see (28a)]. The result appears in Fig. 19, where in addition to the instantaneous expansion $\Theta^{\mathrm{i}}_{\mathrm{ox}}$ at $t = 0$, expansion related to annealing, $\Theta^{\mathrm{i}}_{\mathrm{a}}$, is also seen. Note, that at this temperature, SiO_2 displays viscoelastic behavior. The corresponding material properties appear in Table IV. The final volume changes are presented in Table V.

5.4. Fully Coupled Problem Applied to a Process Sequence

The final example is a numerical solution of two steps out of a typical sequence (involving 10 or more steps) employed in shallow-trench isolation processes. The interested reader is directed to Garikipati *et al.* [24] for a numerical solution of the full process sequence of

TABLE II
Material Properties and Parameters for the Inhomogeneous Expansion Example at $T = 973$ K

Property	Value
κ_{ox}	35.147 GPa
μ_{ox}	30.905 GPa
κ_{Si}	141.67 GPa
μ_{Si}	73.047 GPa

TABLE III
Total and Inelastic Volume Expansion Ratios at T = 973 K

Subdomain	Θ	Θ^{i}_{ox}
Ω_1^+	1.02	1.0
Ω_1^-	1.64	2.2
Ω_2^+	0.989	1.0
Ω_2^-	1.40	2.2

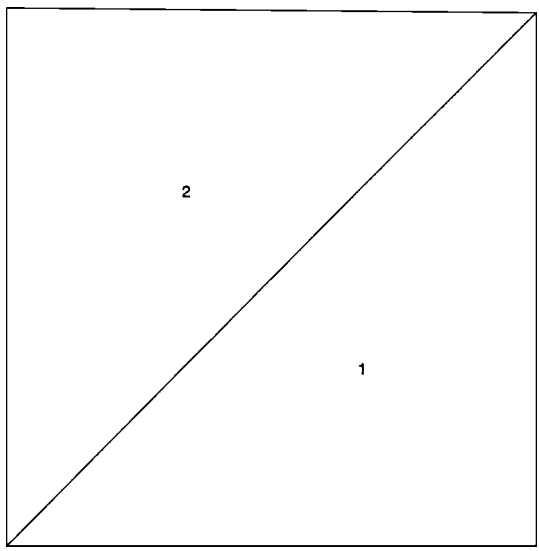

FIG. 17. Initial configuration of two-element mesh, $t = 0^-$.

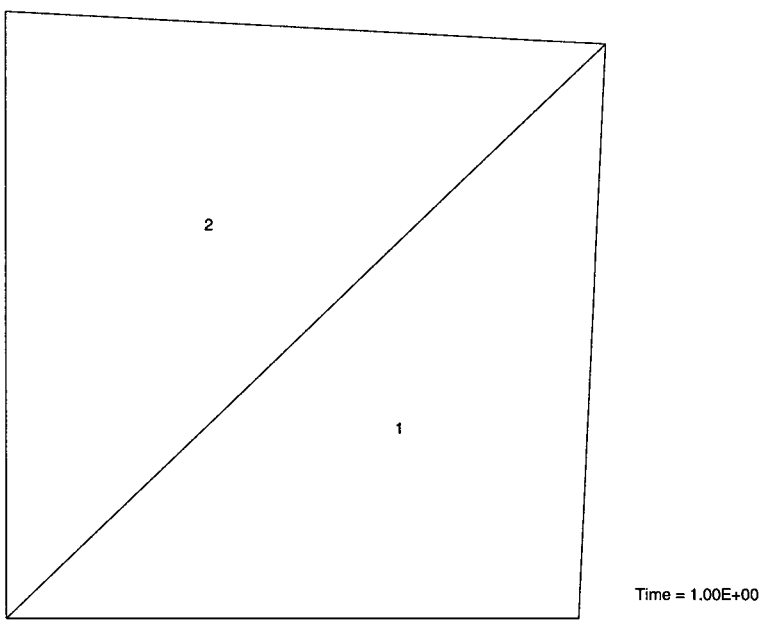

FIG. 18. Expanded configuration at $t = 0^+$.

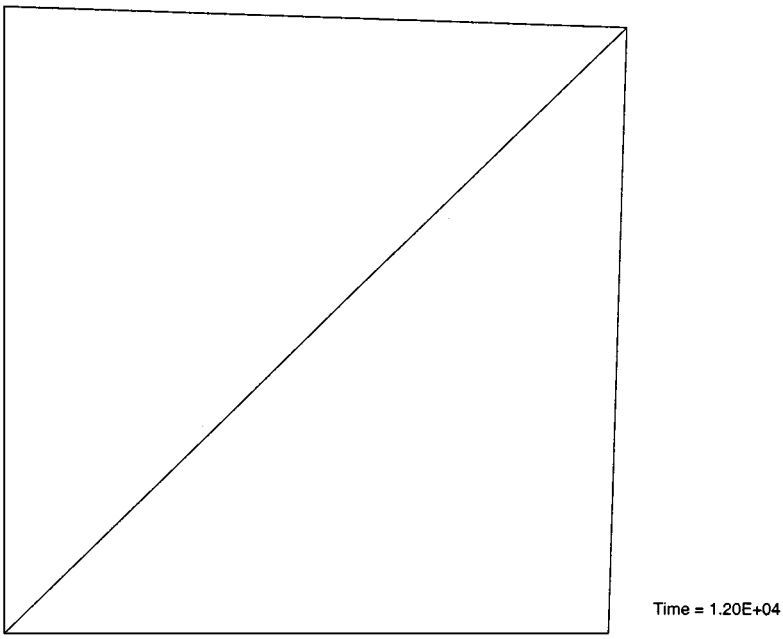

FIG. 19. Expanded configuration at $t = 1.2 \times 10^4$ s.

shallow-trench isolation. Here, the steps considered are (i) thermal oxidation of a trench wall, and (ii) densification following filler deposition.

Figure 20 shows the initial-boundary value problem for the thermal oxidation step. The Si–SiO_2 interface is initially located at a distance of 9 Å from the trench wall and approximately 150 Å below the nitride mask. Figure 21 shows the materials at the start of the oxidation step. The region shown is one-half of a trench structure—itself part of an array of identical trenches. A solution is sought by invoking symmetry boundary conditions on the right- and left-hand boundaries.

The oxidation is carried out at 1373 K and proceeds as follows. (i) Oxidant diffuses through the thin layer of preexisting SiO_2 and reacts at the interface. This leads to the discontinuity in O_2 concentration, the resolution of which is demonstrated in Sections 5.1.1 and 5.1.2. (ii) The formation of native oxide implies movement of the interface into the silicon subdomain (denoted Ω^+). This is achieved by movement of the zero level-set contour

TABLE IV
Material Properties and Parameters for the Inhomogeneous Expansion Example at T = 1323 K

Property	Value
κ_{ox}	12.457 GPa
μ_{ox}	103.82 GPa
γ	0.96959
τ	285.93 s
κ_{Si}	141.67 GPa
μ_{Si}	73.047 GPa

TABLE V

Total and Inelastic Volume Expansion Ratios at $T = 1323$ K

Subdomain	Θ, $t = 0^+$	Θ^i_{ox} at $t = 0^+$	Θ, $t = 1.2 \times 10^4$ s	Θ^i_{ox}, $t = 1.2 \times 10^4$ s	Θ^i_a, $t = 1.2 \times 10^4$ s
Ω_1^+	1.02	1.0	1.02	1.0	1.0
Ω_1^-	1.19	2.2	1.92	2.2	1.0113
Ω_2^+	1.0	1.0	0.999	1.0	1.0
Ω_2^-	1.12	2.2	1.44	2.2	1.0113

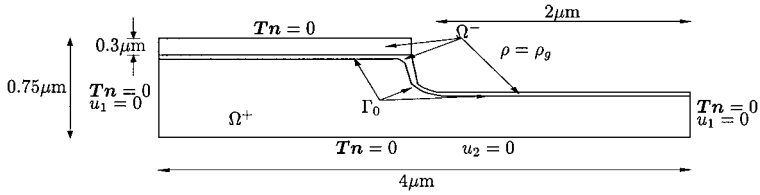

FIG. 20. Problem domain for oxidation of trench wall; $\rho_g = 5 \times 10^{16}$ cm^{-3}.

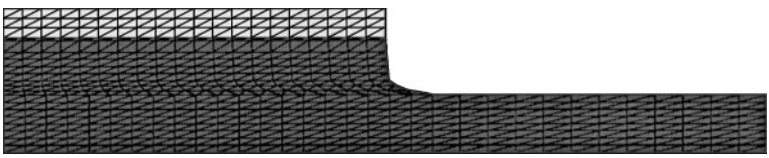

FIG. 21. Materials at the beginning of thermal oxidation of the trench wall: the nitride mask (light gray), silicon substrate (dark gray), and oxide (one-element wide strip of intermediate shade between light and dark gray regions).

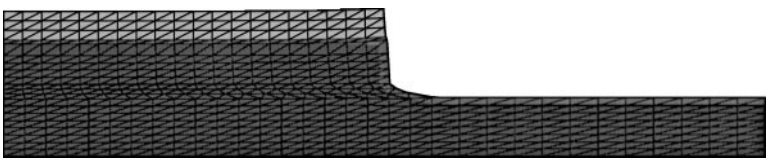

FIG. 22. Materials at the end of thermal oxidation of the trench wall: the nitride mask (light gray), silicon substrate (dark gray), and oxide (light gray region at the trench surface extending to a one-element wide strip between nitride mask and silicon substrate).

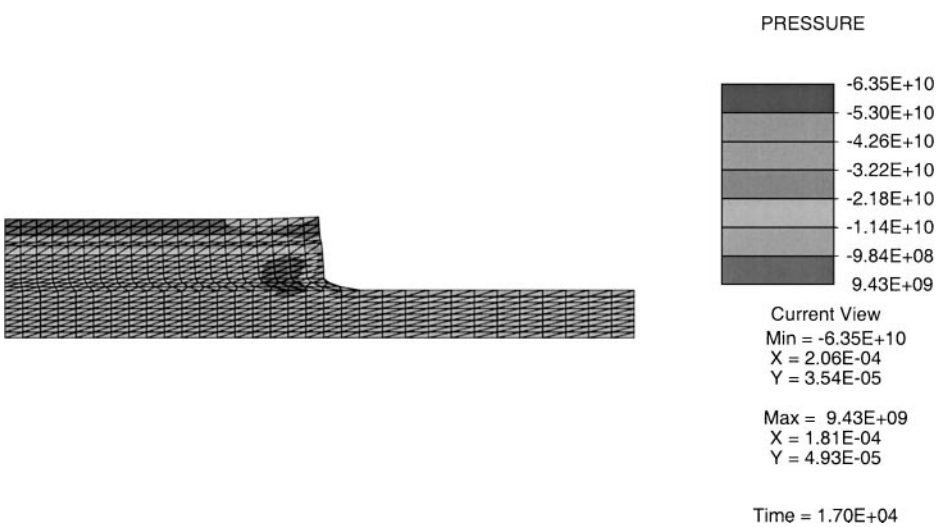

FIG. 23. Pressure contours (dyn-cm^{-2}) at the end of thermal oxidation.

TABLE VI
Material Properties at 1373 K

Property	Value
κ_{ox}	12.158 GPa
μ_{ox}	40.921 GPa
$\gamma_{1_{ox}}$	0.9697
τ_{ox}	132.49 s
κ_{nit}	88.067 GPa
μ_{nit}	61.415 GPa
$\gamma_{1_{nit}}$	0.9697
τ_{nit}	2926.9 s
κ_{Si}	141.67 GPa
μ_{Si}	73.047 GPa
$D_{0_{ox}}$	1.3786×10^{-6} cm^2/s
k_{s0}	-7.8752×10^{-3} cm/s
$D_{0_{nit}}$	1.0×10^{-14} cm^2/s
$D_{0_{Si}}$	1.3786×10^{-8} cm^2/s
α_{ox}	5.5×10^{-7}
α_{nit}	1.0×10^{-6}
α_{Si}	3.0×10^{-6}

(Section 5.2). (iii) The newly formed SiO_2 instantaneously expands by a ratio Θ^{i}_{ox}, while the preexisting SiO_2 continues to expand to a ratio Θ^{i}_{a}. The quasistatic stress-equilibrium problem is solved. The solution proceeds as described in Section 4.4.

Figure 22 shows the different materials at the end of 360 s. The lining of oxide on the trench wall has grown. The nitride (Si_3N_4) serves as a mask against diffusion of oxidant, thereby preventing further oxidation of the silicon just below it. The standard solid viscoelastic model has been employed for the nitride as well. All material properties at this temperature appear in Table VI. In this step of the shallow-trench isolation sequence the oxide lining on the trench wall is grown in preparation for the next step, wherein oxide will be deposited in the trench. The oxide serves to isolate active silicon regions in the structure from each other. The growth of oxide, which expands, leads to generation of large stresses due to the associated inelastic strain Θ^{i}_{ox}. Additionally, there are stresses associated with the mismatch of thermal expansion coefficients (denoted α_{ox}, α_{nit}, and α_{Si} in Table VI) between dissimilar materials. Figure 23 shows the pressure in terms of the Cauchy stress, $p = (1/3)\boldsymbol{\sigma} : \mathbf{1}$. Stress concentrations are seen under the tip of the nitride mask in the trench's upper corner. These results correspond well with experimental measurements of stress in the silicon obtained from micro-Raman spectroscopy (see Garikipati *et al.* [24]).

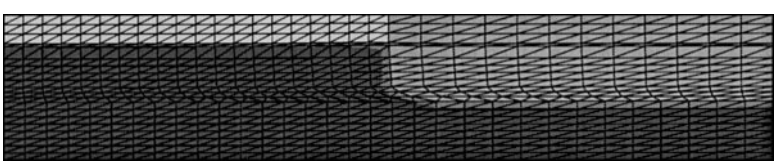

FIG. 24. Materials at the end of annealing following filling of the trench: the nitride mask (light gray region at the top left), silicon substrate (bottom dark gray region), deposited oxide (light gray region at top right), and thermally-grown oxide (light gray region separating the silicon substrate from nitride mask and deposited oxide).

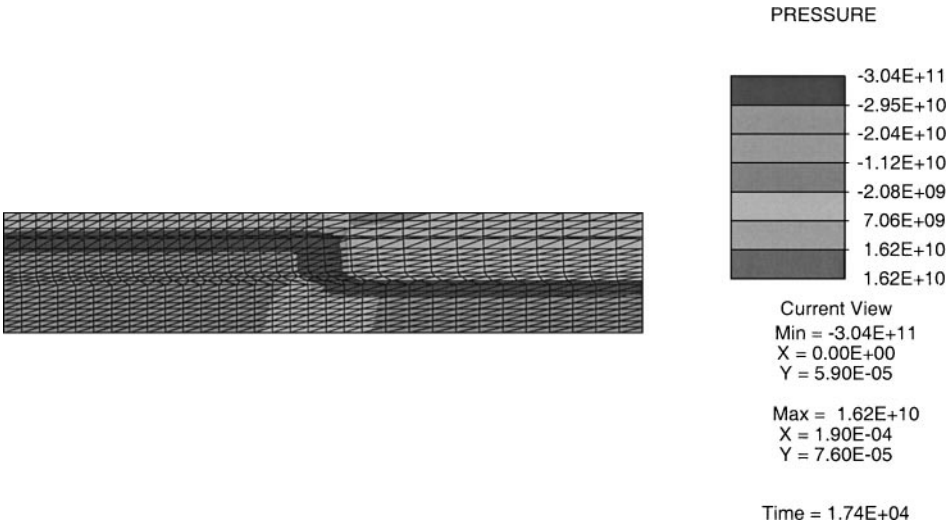

FIG. 25. Pressure contours (dyn-cm^{-2}) at the end of the annealing stage.

In the actual process, the next step involves deposition of tetraethoxysilane (TEOS) in the trench. Reactions take place leading to the formation of SiO_2. The filling of the trench is modeled by activating the finite-element mesh in the trench region (this portion of the mesh was deactivated for the previous step) and ascribing properties of SiO_2 to it. We consider an isothermal annealing of the structure at 1073 K leading to an inelastic volume expansion Θ_a^i of SiO_2 formed by either thermal oxidation or deposition (Section 3.2). The process flow involves annealing in an inert ambient. Accordingly, the concentrations remain fixed at the values attained at the end of oxidation and the interface does not evolve. The staggered solution of the fully coupled problem can hence be abandoned and the mechanical problem alone needs to be solved. Figure 24 shows the materials corresponding to this stage and Fig. 25 is a plot of the pressure, p, at the end of 300 s of annealing. The inelastic expansion of SiO_2 in the trench and trench wall lead to compressive stress in the silicon substrate. This result also corresponds well with the micro-Raman spectroscopy measurements referred to above.

6. CONCLUSION

The mathematical, mechanical, and numerical models described in Rao and Hughes [1] and Rao *et al.* [2] represent important advances over the preexisting state of thermal oxidation models. However, as pointed out in Section 1, several improvements were possible. These have been discussed at length in the present work. In the case of the level-set method for interface movement these included the development of a velocity projection scheme and application of recent spatial stabilization methods. The diffusion-reaction equation benefited from an imposition of the positivity constraint for concentration in the presence of discontinuities. These are largely implementational and numerical issues. However, the mechanics has been enhanced by the introduction of an additional phenomenological model for annealing-induced oxide expansion. The expansion-related changes have been formulated in an inelastic setting and the accompanying irreversible thermodynamics has been

elucidated. Explicit evolution equations for the components of inelastic volumetric strains have been stated. This provides a greater measure of rigor to the mechanics. Inhomogeneous expansion of elements that contain the interface and hence are part silicon and part SiO_2 is made possible in the framework of the enhanced strain finite-element method. This makes the solution of the mechanics problem more robust.

Some additional experimental data is currently being sought on viscoelastic properties of various types of SiO_2 films and the annealing-induced expansion. These are discussed by Garikipati *et al.* [24]. The formulation of the fully coupled thermomechanical problem is relevant to the accurate modeling of the high thermal heating rates used in semiconductor manufacturing processes. This and the extension of the models to three dimensions are important steps that will form the subject of future publications.

ACKNOWLEDGMENTS

Support for this work was provided by Advanced Micro Devices, Inc., and the Center for Integrated Systems, Stanford University.

REFERENCES

1. V. S. Rao and T. J. R. Hughes, On modelling thermal oxidation of silicon. I: Theory, *Int. J. Numer. Methods Eng.* **47**(1/3), 341 (2000).
2. V. S. Rao, T. J. R. Hughes, and K. Garikipati, On modelling thermal oxidation of silicon. II: Numerical aspects, *Int. J. Numer. Methods Eng.* **47**(1/3), 359 (2000).
3. C. S. Rafferty, *Stress Effects in Silicon Oxidation—Simulation and Experiments*, Ph.D. thesis (Stanford Univ., 1989).
4. J. P. Peng, D. Chidambarrao, and G. R. Srinivasan, Novel. A nonlinear viscoelastic model for thermal oxidation of silicon, *COMPEL* **10**(4), 341 (1991).
5. V. Senez, D. Collard, P. Ferreira, and B. Baccus, Two-dimensional simulation of local oxidation of silicon: Calibrated viscoelastic flow analysis, *IEEE Trans. Electron. Dev.* **43**(8), 720 (1996).
6. T. Uchida, M. Fujinaga, N. Kotani, S. Kawazu, and H. Miyoshi, Stable solution method for viscoelastic oxidation including stress-dependent viscosity, *Jpn. J. Appl. Phys.* **35**(8), 4265 (1996).
7. S. Cea and M. E. Law, Three dimensional nonlinear viscoelastic oxidation modeling, in *International Conference on Simulation of Semiconductor Processes and Devices, SISPAD, IEEE, Tokyo, Japan* (1996), pp. 97–98.
8. H. A. Rueda, S. Cea, and M. E. Law, Mechanical stress modeling for silicon fabrication processes, in *International Conference on Simulation of Semiconductor Processes and Devices, SISPAD, IEEE, Piscataway, NJ, USA* (1997), pp. 53–56.
9. J. A. Sethian, *Level Set Methods* (Cambridge Univ. Press, Cambridge, UK, 1996).
10. J. A. Sethian and D. Adalsteinsson, An overview of level set methods for etching, deposition and lithography development, *IEEE Trans. Semicond. Man.* **10**(1), 167 (1997).
11. D. Chin, *Two-Dimensional Oxidation*, Ph.D. thesis (Stanford Univ., 1983).
12. C. H. Hsueh and A. G. Evans, Oxidation induced stress and some effects on the behavior of oxide films, *J. Appl. Phys.* **54**(11) (1983).
13. M. J. Needs, V. Jovic, C. Taylor, K. Board, and M. J. Cooke, A 2d linear elastic model for the local oxidation of silicon using the boundary element method, in *Proceedings of the 2nd Conference on Simulation of Semiconductor Devices and Processes* (1986), p. 412.
14. S. M. Hu, Stress-related problems in silicon technology, *J. Appl. Phys.* **70**(6), R53 (1991).
15. P. M. Fahey, S. R. Mader, S. R. Stiffler, R. L. Mohler, J. D. Mis, and J. A. Slinkman, Stress-induced dislocations in silicon integrated circuits, *IBM J. Res. Dev.* **36**(2), 158 (1992).

16. M. Navi and S. T. Dunham, Viscous compressible model for stress generation/relaxation in SiO_2, *J. Electrochem. Soc.* **144**(1), 367 (1997).
17. C. L. Yu, P. A. Flinn, and J. C. Bravman, In-situ measurement of viscous flow of thermal silicon dioxide thin films at high temperature, in *Amorphous and Crystalline Insulating Thin Films*, edited by W. L. Warren, R. A. B. Devine, M. Matsumura, S. Cristoloveanu, Y. Homma, and J. Kanicki (Materials Res. Soc., Pittsburgh, 1996), pp. 261–266.
18. E. P. EerNisse, Stress in thermal SiO_2 during growth, *Appl. Phys. Lett.* **35**(1), 8 (1979).
19. N. B. Pilling and R. E. Bedworth, *J. Inst. Metall.* **29**, 529 (1923).
20. D. A. Vermilyea, On the mechanism of the oxidation of metals, *Acta Metall.* **5**, 492 (1957).
21. C. L. Yu, P. A. Flinn, and J. C. Bravman, In-situ stress measurements during dry oxidation of silicon, in *Materials Reliability in Microelectronics VII*, edited by J. E. Sanchez, R. R. Keller, K. S. Krisch, and Z. Suo (Materials Res. Soc., Pittsburgh, 1997), pp. 95–100.
22. G. G. Stoney, The tension of metallic films deposited by electrolysis, *Proc. R. Soc. London Ser. A* **82**, 172 (1909).
23. J. C. Simo and T. J. R. Hughes, *Computational Inelasticity* (Springer-Verlag, New York, 1998).
24. K. Garikipati, V. S. Rao, M. Y. Hao, E. Ibok, I. DeWolf, and R. W. Dutton, Modelling and validation of contributions to stress in the shallow trench isolation process sequence, *Comp. Model. Eng. Sci.* **1**(1), 63 (2000).
25. T. Barth and J. A. Sethian, Numerical schemes for the hamilton-jacobi and level set equations on triangulated domains, *J. Comput. Phys.* **145**(1), 1 (1998).
26. J. C. Simo, R. L. Taylor, and K. S. Pister, Variational and projection methods for the volume constraint in finite deformation plasticity, *Comp. Methods Appl. Mech. Eng.* **51**, 177 (1985).
27. J. C. Simo, On a fully three-dimensional finite strain viscoelastic damage model: Formulation and computational aspects. *Comp. Methods Appl. Mech. Eng.* **60**, 153 (1985).
28. S. R. Rekhson, Viscoelastic relaxation, in *Glass-Science and Technology: Viscosity and Relaxation*, edited by D. R. Uhlmann and N. J. Kreidl (Academic, New York, 1986), Vol. 3.
29. P. G. Ciarlet, *Mathematical Elasticity* (North-Holland, Amsterdam, 1993).
30. E. A. Irene, E. Tierney, and J. Angilello, A viscous flow model to explain the appearance of high density thermal SiO_2 at low oxidation temperatures, *J. Electrochem. Soc.* **129**, 2594 (1982).
31. R. De Hoff, *Thermodynamics in Materials Science* (McGraw-Hill, New York, 1993).
32. K. Taniguchi, M. Tanaka, and C. Hamaguchi, Density relaxation of silicon dioxide on (100) silicon during thermal annealing, *J. Appl. Phys.* **67**(5), 2195 (1990).
33. C. A. Truesdell and W. Noll, *The Nonlinear Field Theories of Mechanics*, Number III/3 in *Handbuch der Physik* (Springer-Verlag, New York, 1965).
34. C. S. Rafferty, L. Borucki, and R. W. Dutton, Plastic flow during thermal oxidation of silicon, *Appl. Phys. Lett.* **54**(16), 1516 (1989).
35. S. J. Fenves, N. Perrone, A. R. Robinson, and W. C. Schnobrich, editors, *Incompatible Displacement Models* (Academic, New York, 1973).
36. R. L. Taylor, P. J. Beresford, and E. L. Wilson, A non-conforming element for stress analysis. *Int. J. Numer. Methods Eng.* **10**(6), 1211 (1976).
37. J. C. Simo and M. S. Rifai, A class of mixed assumed strain methods and the method of incompatible modes, *Int. J. Numer. Methods Eng.* **29**, 1595 (1990).
38. N. Moës, J. Dolbow, and T. Belytschko, A finite element method for crack growth without remeshing, *Int. J. Numer. Methods Eng.* **46**, 131 (1999).
39. A. N. Brooks and T. J. R. Hughes, Streamline upwind/Petrov-Galerkin formulations for convection dominated flows with particular emphasis on the incompressible Navier-Stokes equations, *Comp. Methods Appl. Mech. Eng.* **32**, 199 (1982).
40. T. J. R. Hughes and M. Mallet, A new finite element formulation for computational fluid dynamics. III. The generalized streamline operator for multidimensional advective-diffusive flows, *Comp. Methods Appl. Mech. Eng.* **58**(3), 305 (1986).

41. T. J. R. Hughes, L. Franca, and M. Mallet, A new finite element formulation for computational fluid dynamics. VII. Convergence analysis of the generalized SUPG formulation for linear time-dependent multidimensional advective-diffusive systems, *Comp. Methods Appl. Mech. Eng.* **63**(1), 97 (1987).
42. T. J. R. Hughes, L. Franca, and G. M. Hulbert, A new finite element formulation for computational fluid dynamics. VIII. The Galerkin/least-squares methods for advective-diffusive equations, *Comp. Methods Appl. Mech. Eng.* **73**, 173 (1989).
43. Z. Johan, T. J. R. Hughes, and F. Shakib, A globally convergent matrix-free algorithm for implicit time-marching schemes arising in finite element analysis in fluids, *Comp. Methods Appl. Mech. Eng.* **87**, 281 (1991).
44. F. Brezzi and A. Russo, Choosing bubbles for advection-diffusion problems, *MMMAS* **4**(4), 571 (1994).
45. T. J. R. Hughes, Multiscale phenomena; Green's functions, the Dirichlet-to-Neumann formulation, subgrid scale models, bubbles and the origins of stabilized methods, *Comp. Methods Appl. Mech. Eng.* **127**, 387 (1995).
46. M. Stolarska, D. L. Chopp, N. Moës, and T. Belytschko, Modelling crack growth by level sets in the extended finite element method, *Int. J. Numer. Methods Eng.* **51**, 943 (2001).
47. J. C. Simo and F. Armero, Geometrically nonlinear enhanced mixed finite element methods and the method of incompatible modes. *Int. J. Numer. Methods Eng.* **33**, 1413 (1992).
48. J. C. Simo, F. Armero, and R. L. Taylor, Improved versions of assumed enhanced strain tri-linear elements for 3d finite deformation problems. *Comp. Methods Appl. Mech. Eng.* **110**, 359 (1993).
49. S. Glaser and F. Armero, On the formulation of enhanced strain finite elements in finite deformations, *Eng. Comput.* **14**(6–7), 759 (1997).
50. F. Armero and K. Garikipati, An analysis of strong discontinuities in multiplicative finite strain plasticity and their relation with the numerical simulation of strain localization in solids, *Int. J. Solids Struct.* **33**(20–22), 2855 (1996).
51. R. L. Taylor, J. C. Simo, O. C. Zienkiewicz, and A. C. Chan, The patch test: A condition for assessing finite element convergence, *Int. J. Numer. Methods Eng.* **22**, 39 (1986).